

ViP²-CLIP: Visual-Perception Prompting with Unified Alignment for Zero-Shot Anomaly Detection

Ziteng Yang^{1*} Jingzehua Xu^{1*} Yanshu Li^{2*} Zepeng Li¹ Yeqiang Wang¹ Xinghui Li^{1†}

¹Tsinghua University ²Brown University

Abstract

Zero-shot anomaly detection (ZSAD) aims to detect anomalies without any target domain training samples, relying solely on external auxiliary data. Existing CLIP-based methods attempt to activate the model’s ZSAD potential via handcrafted or static learnable prompts. The former incur high engineering costs and limited semantic coverage, whereas the latter apply identical descriptions across diverse anomaly types, thus fail to adapt to complex variations. Furthermore, since CLIP is originally pretrained on large-scale classification tasks, its anomaly segmentation quality is highly sensitive to the exact wording of class names, severely constraining prompting strategies that depend on class labels. To address these challenges, we introduce ViP²-CLIP. The key insight of ViP²-CLIP is a Visual-Perception Prompting (ViP-Prompt) mechanism, which fuses global and multi-scale local visual context to adaptively generate fine-grained textual prompts, eliminating manual templates and class-name priors. This design enables our model to focus on precise abnormal regions, making it particularly valuable when category labels are ambiguous or privacy-constrained. Extensive experiments on 15 industrial and medical benchmarks demonstrate that ViP²-CLIP achieves state-of-the-art performance and robust cross-domain generalization.

1. Introduction

Large-scale vision-language models (VLMs) such as CLIP [26] have shown impressive zero-shot recognition capabilities by pre-training on vast image-text pairs. Inspired by this success, CLIP has been widely adopted for Zero-Shot Anomaly Detection (ZSAD) [14], which seeks to detect anomalies automatically without any target domain training samples, offering a practical solution for data-scarce scenarios. Unlike conventional image classification, which focuses on foreground semantics, anomaly detection emphasizes irregular regions on object surfaces. Consequently, existing CLIP-based ZSAD methods typically construct two

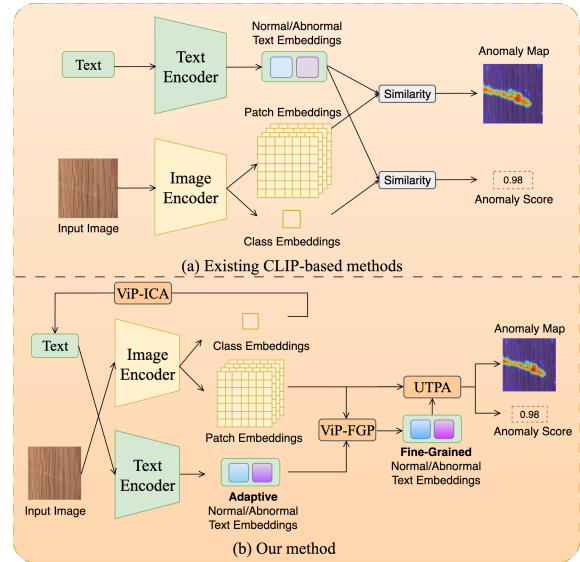


Figure 1. Comparison between prior CLIP-based methods and ViP²-CLIP. ViP²-CLIP introduces ViP-Prompt to replace fixed class-name tokens with image-conditioned prompts that fuse global and local cues, and it first employs a unified patch-level alignment within training-based CLIP models.

sets of text prompts—‘normal’ and ‘anomalous’, and align them with image features in a shared semantic space. As illustrated in Fig. 1 (a), text prompts are aligned with the global image feature to infer image-level anomaly score, while alignment with local patch features then generates pixel-level anomaly maps.

Currently, state-of-the-art ZSAD methods focus on prompt engineering to leverage CLIP’s generalization. Representative approaches such as WinCLIP [14], Anomaly-CLIP [37], and VCP-CLIP [25] either craft semantically rich manual templates or learn prompt tokens to boost performance. However, manual templates demand extensive human effort and cannot guarantee comprehensive semantic coverage. Although some works [37] introduce object-agnostic learnable prompts to capture generic normal and abnormal concepts, they apply the same description across

diverse anomaly types, hindering adaptability to complex semantic variations. Moreover, methods like CLIP-AD [6], AdaCLIP [4], FILo [10], KANOCLIP [19], and AA-CLIP [22] rely heavily on class names as prompt priors. Yet we find that CLIP’s segmentation quality remains acutely sensitive to semantically equivalent class-name variations, even after fine-tuning on auxiliary anomaly data (see Appendix A for detailed analysis). This likely stems from the limited scope of downstream adaptation, which cannot fully stabilize local alignment against label shifts. Such sensitivity constrains the class-name usage in prompts, highlighting the urgent need for robust, class-name agnostic but adaptive prompting strategies in ZSAD.

To this end, we propose a Visual-Perception Prompting (ViP-Prompt) mechanism composed of an Image-Conditioned Adapter (ICA) and a Fine-Grained Perception Module (FGP). ICA adaptively injects global visual context into the prompts’ embedding space, while FGP integrates multi-scale patch features, enabling the prompts to capture fine-grained irregularities. By replacing fixed class-name tokens with image-conditioned prompts that fuse global and local cues, ViP-Prompt significantly enhances prompts’ robustness and reinforces cross-modal alignment across diverse semantic scenarios. Building upon that, we further introduce ViP²-CLIP, a ZSAD model that integrates visual-perception prompts with a unified alignment mechanism; its overall architecture is depicted in Fig. 1 (b). ViP²-CLIP first employs ViP-Prompt to condition text prompts on both global and local visual cues, fully leveraging CLIP’s ZSAD performance; it then adopts a Unified Text-Patch Alignment (UTPA) strategy to align prompt tokens with multi-scale patch features through a single optimization, yielding superior precision in both detection and localization.

Our key contributions are summarized as follows:

- We propose ViP-Prompt, which fuses global and local visual features to generate image-conditioned prompts, fully exploiting CLIP’s potential for ZSAD. This design eliminates the need for handcrafted templates or class-name priors, delivers stronger generalization and robustness, making it particularly valuable when category labels are ambiguous or privacy-constrained.
- On top of that, we present ViP²-CLIP, which integrates a simple but effective strategy-UTPA, that for the first time, introduces a consistency-alignment strategy within training-based CLIP models, enhancing CLIP’s performance in both anomaly detection and localization.
- Comprehensive experiments on 15 industrial and medical datasets demonstrate that ViP²-CLIP consistently achieves superior ZSAD performance.

2. Related Work

Zero-Shot Anomaly Detection (ZSAD) ZSAD localizes abnormal regions without any target class samples during training. The advent of CLIP [26] has spurred notable advances in this task. WinCLIP [14] first ported CLIP to ZSAD with diverse handcrafted prompts. However, since CLIP is pretrained to align with general object semantics rather than abnormal patterns, its anomaly detection capability remains limited. To ease this burden, APRIL-GAN [5] and CLIP-AD [6] append shallow linear heads and fine-tune them on auxiliary datasets. AnomalyCLIP [37] removes handcrafted templates via learnable, object-agnostic prompts, boosting cross-domain generalization, while AdaCLIP [4] employs hybrid prompts to align text and image features better. VCP-CLIP [25] instead projects the image’s global feature into a fixed handcrafted prompt space, which enhances segmentation performance. AA-CLIP [22] adopted a two-stage training strategy that separately optimizes text and image encoders to encourage greater divergence in the text embedding space for improved anomaly discrimination. AF-CLIP [9] further integrated multi-scale feature aggregation to improve detection performance.

Prompt Learning Prompt learning was initially proposed in natural language processing to enhance the adaptability of pre-trained models [24, 32] to diverse downstream tasks. CoOp [26] first brought this paradigm to the vision domain by inserting trainable tokens into text inputs, allowing CLIP to adapt to specific tasks without fine-tuning. Static prompts, however, soon proved brittle on unseen classes. To enhance transferability, CoCoOp [36] and DenseCLIP [27] generate image-conditioned prompts that respond to visual context. Recent works [34, 35] enforce prompt generalization by regularizing learnable tokens toward handcrafted templates, improving unseen class recognition. Works as MaPL [17], PromptSRC [18] and MMRL [11] push prompting into both modalities, jointly tuning image and text space for more substantial cross-modal alignment.

3. Preliminary

CLIP consists of a text encoder $T(\cdot)$ and a visual encoder $F(\cdot)$, both implemented as mainstream multi-layer networks. Leveraging contrastive learning on large-scale image-text pairs, CLIP achieves superior zero-shot recognition. Given a class name c , we combine it with a text prompt template G (e.g., ‘A photo of a [cls]’, where [cls] represents the category class-name). The resulting text is then fed into the text encoder $T(\cdot)$ to obtain the prompt embedding $g_c = T(G(c)) \in \mathbb{R}^D$. For an input image x_i , the visual encoder generates its global visual embedding $f_i \in \mathbb{R}^D$ and the local patch embeddings $f_i^m \in \mathbb{R}^{H \times W \times D}$. Specifically, given a category set C , CLIP computes the probability of

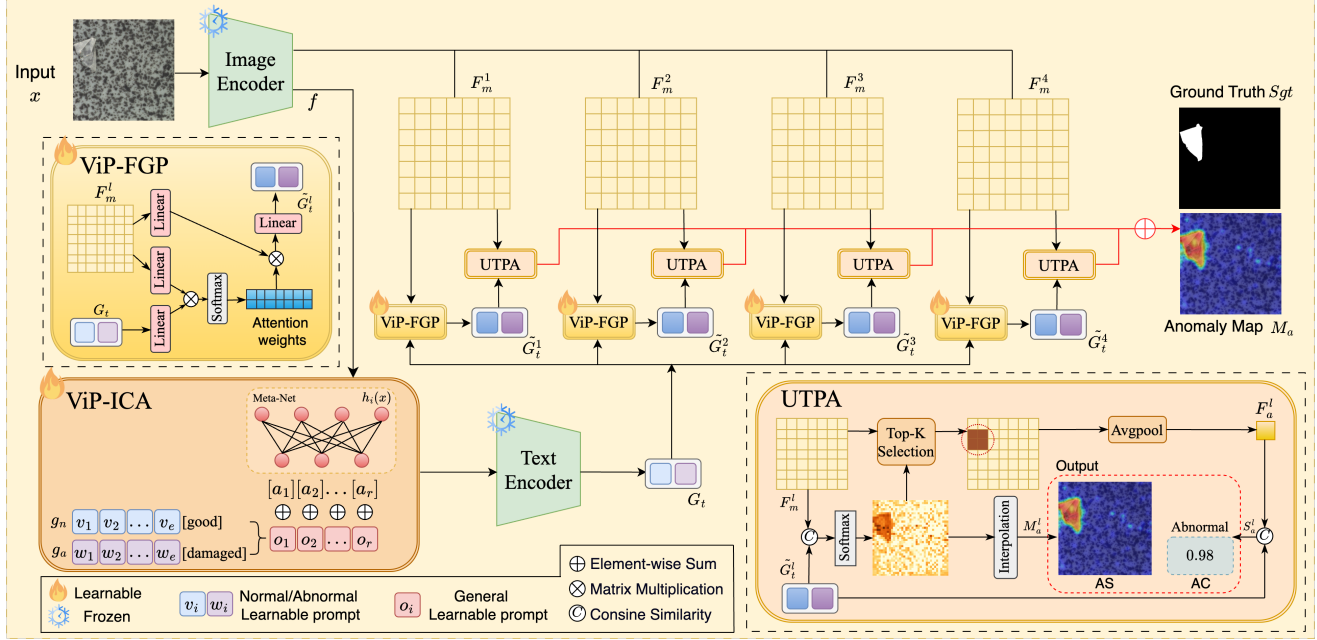


Figure 2. Framework of ViP²-CLIP. ViP²-CLIP first introduces ViP-Prompt to enhance cross-modal alignment: ViP-ICA injects global visual context into the prompts’ embedding space, while ViP-FGP fuses local patch features to enhance the prompts’ fine-grained perceptual capacity. Finally, the UTPA module performs unified alignment in multiple layers to jointly support image-level anomaly detection and pixel-level anomaly localization.

image x_i belonging to c as follows:

$$p(y = c | x_i) = P(g_c, f_i) = \frac{\exp(\langle g_c, f_i \rangle / \tau)}{\sum_{c' \in C} \exp(\langle g_{c'}, f_i \rangle / \tau)}, \quad (1)$$

where τ is a temperature hyperparameter and $\langle \cdot, \cdot \rangle$ denotes the cosine similarity.

Unlike conventional classification, ZSAD flags deviations from normality rather than assigning foreground semantics. Most approaches, therefore, instantiate two text prompts [14], a normal prompt g_n and an abnormal prompt g_a . At the image level, they compare the global image feature f_i with both prompts and take $P(g_a, f_i)$ as the anomaly score; while at the pixel level, for each location (j, k) , they extract the patch token $f_i^m(j, k)$, and compute the local normal score $S_n(j, k) = P(g_n, f_i^m(j, k))$ and anomaly score $S_a(j, k) = P(g_a, f_i^m(j, k))$, from which a pixel-wise anomaly map is generated.

4. Method

We propose ViP²-CLIP, which leverages Visual-Perception Prompting (ViP-Prompt) to fully exploit CLIP’s ZSAD capabilities. As illustrated in Fig. 2, ViP²-CLIP first introduces ViP-Prompt (Sec. 4.1) to fuse learnable normal and abnormal prompts with both global and multi-scale local visual features. This design enables prompts to adaptively capture the fine-grained visual patterns of the in-

spected image, thereby improving cross-modal semantic alignment. Furthermore, we adopt a Unified Text-Patch Alignment (UTPA) scoring strategy (Sec. 4.2), which optimizes alignment between prompt tokens and multi-scale patch features to support anomaly detection and localization jointly. By aggregating alignment signals across multiple layers, ViP²-CLIP produces robust anomaly scores and fine-grained anomaly maps.

4.1. Visual-Perception Prompt (ViP-Prompt)

We propose ViP-Prompt, an adaptive fine-grained prompting framework, which is built from an Image-Conditioned Adapter (ICA) and Fine-Grained Perception Module (FGP). By fusing learnable tokens with the global and local visual context, ViP-Prompt generates multi-level descriptions that flexibly track objects’ visual patterns, thus markedly exploiting CLIP’s ZSAD performance in diverse scenarios.

Image-Conditioned Adapter (ICA) To eliminate dependence on handcrafted templates and class-name priors, we first define static learnable prompt templates for both normal and anomaly classes:

$$g_n = [v_1][v_2] \dots [v_e] \text{ good } [o_1] \dots [o_r], \quad (2)$$

$$g_a = [w_1][w_2] \dots [w_e] \text{ damaged } [o_1] \dots [o_r], \quad (3)$$

here, $\{v_i\}, \{w_i\} \in \mathbb{R}^C$ denote the learnable normal and anomaly vector, respectively. $\{o_i\} \in \mathbb{R}^C$ is a generic

learnable token that replaces the explicit class label. We adopt the adjectives ‘good’ and ‘damaged’ to guide the prompts to learn richer normal and anomalous semantics. By autonomously learning g_n and g_a , the model can capture generic anomaly patterns across diverse objects.

To condition prompts on the target object and thus adapt to complex detection scenarios, we map the global visual embedding f extracted by the image encoder through a lightweight Meta-Net $h_i(\cdot)$ (Linear-ReLU-Linear) into the text embedding space, denoted as $\{a_i\}_{i=1}^r = h_i(f)$, where r is the number of mapped tokens and $a_i \in \mathbb{R}^C$, then fuse it with static learnable vector to generate dynamic prompt token. Thus, we define the prompts’ structure as follows:

$$g_n = [v_1][v_2] \dots [v_e] \text{ good } [z_1] \dots [z_r], \quad (4)$$

$$g_a = [w_1][w_2] \dots [w_e] \text{ damaged } [z_1] \dots [z_r], \quad (5)$$

where $z_i = o_i + a_i$. By projecting the image’s global feature into the text embedding space, ICA adaptively generates normal and anomalous descriptors conditioned on the target object, eliminating the dependence on explicit class labels and enabling more robust cross-modal alignment in privacy-constrained settings.

Fine-Grained Perception Module (FGP) To further enhance the prompts’ fine-grained perceptual capacity, we introduce an attention-based interaction module between the text prompts and multi-scale visual features. Specifically, we project both text embeddings and local patch embeddings into a shared C -dimension space. Let $G_t \in \mathbb{R}^{2 \times C}$ be the prompt embeddings from the text encoder, and $F_m^l \in \mathbb{R}^{HW \times D}$ be the smoothed local visual embeddings from the l -th layer of the visual encoder, we then apply three learnable linear mappings to produce query $Q_t = G_t W_q$, key $K_m^l = F_m^l W_k$, and value $V_m^l = F_m^l W_v$, where $W_q \in \mathbb{R}^{C \times C}$, $W_k, W_v \in \mathbb{R}^{D \times C}$, are learnable projection matrices.

Then, we compute scaled dot-product attention via $\text{Softmax}(Q_t K_m^{l\top} / \sqrt{C})$, and apply these weights to the values V_m^l , yielding enhanced token embeddings. Finally, a linear projection $W_o \in \mathbb{R}^{C \times D}$ transforms these embeddings into the layer-specific prompts \tilde{G}_t^l , which integrate fine-grained local features:

$$\tilde{G}_t^l = (\text{Softmax}(Q_t K_m^{l\top} / \sqrt{C}) V_m^l) W_o, \quad (6)$$

here, $\tilde{G}_t^l \in \mathbb{R}^{2 \times D}$ comprises the fine-grained normal prompt \tilde{g}_n and anomalous prompt \tilde{g}_a .

To assess FGP’s fine-grained sensitivity, Fig. 3 visualizes the attention maps of both normal and abnormal prompts across diverse images. Normal prompts activate on regular textures and structures of the image, while anomalous

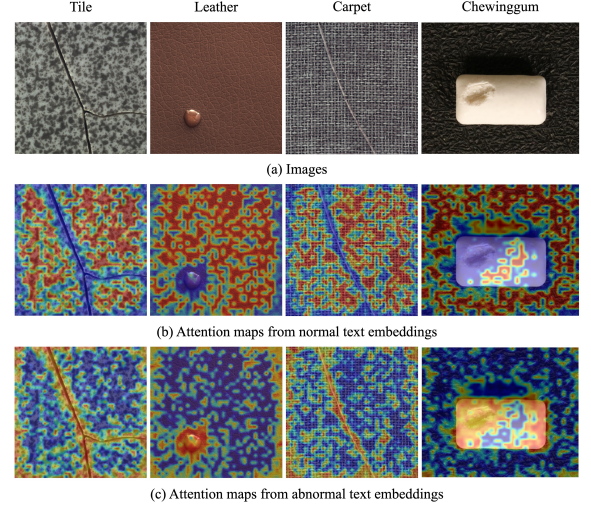


Figure 3. Visualization results of the attention maps from different prompts in our FGP module.

prompts concentrate on defects and irregular regions, indicating high sensitivity to anomalous patterns. These results demonstrate that FGP effectively refines prompt embeddings by incorporating localized visual cues, thereby enhancing cross-modal alignment.

4.2. Unified Text-Patch Alignment (UTPA)

Recent CLIP-based ZSAD models typically adopt a dual-branch alignment scheme [5, 6, 37]: one branch aligns the text prompt with global visual embedding to score anomalies at the image level, while the other aligns it with local patch embeddings for pixel-level anomaly maps. However, because these branches operate in separate feature subspaces, it hinders the simultaneous attainment of high-precision anomaly detection and localization.

To address this limitation, we introduce the UTPA strategy, which treats anomaly detection and localization as a unified alignment task between text embeddings and local patch embeddings. Concretely, to obtain the pixel-level anomaly map, we follow the standard practice: for the l -th layer feature map F_m^l , the patch token at spatial location (j, k) , denoted as $f_{j,k}^l \in \mathbb{R}^D$, receives its anomaly score by computing the similarity $P(\tilde{g}_a, f_{j,k}^l)$, as defined in Eq. (1).

Next, we upsample the anomaly scores of all patch tokens to produce the anomaly map M_a^l :

$$M_a^l = \text{Up}(P(\tilde{g}_a, F_m^l)), \quad (7)$$

where $\text{Up}(\cdot)$ denotes channel-wise upsampling.

Unlike prior works [5, 6, 37] that rely on global alignment, we contend that an image’s abnormality is driven by its most defective regions. Consequently, our image-level score is still derived from local patch features. For the l -th layer feature map F_m^l , we select the Top-k patch tokens

with the highest $P(\tilde{g}_a, f_{j,k}^l)$ among all patches. The image’s representative anomaly feature F_a^l is then obtained via global average pooling over this subset:

$$F_a^l = \frac{1}{k} \sum_{(j,k) \in \mathcal{T}_l} f_{j,k}^l, \quad (8)$$

where \mathcal{T}_l indexes the chosen Top-k patches. The Top-k pooling directs the model’s attention to the most suspicious patches, ensuring that the subsequent anomaly score faithfully reflects the severity of localized defects. Consequently, the image-level anomaly score S_a^l at the l -th layer is obtained by computing $S_a^l = P(\tilde{g}_a, F_a^l)$. By enforcing a unified text-patch alignment, UTPA effectively overcomes the optimization conflict of traditional dual-branch schemes, yielding more balanced ZSAD performance, as further validated in Sec. 5.3.

4.3. Training and Inference

During training, ViP²-CLIP is optimized by minimizing a global loss L_{global} and a local loss L_{local} [37]:

$$L_{\text{total}} = L_{\text{global}} + \lambda \sum_{l=1}^N L_{\text{local}}^{M^l}, \quad (9)$$

here, λ is a hyperparameter to balance the global and local losses; N represents the number of intermediate layers. L_{global} is the cross-entropy loss matching the cosine similarity between text embeddings \tilde{g}_n/\tilde{g}_a and the representative anomalous visual feature F_a^l ; L_{local} is computed as the sum of a Focal loss [21] and a Dice loss [20] to optimize local alignment jointly:

$$\begin{aligned} L_{\text{local}} = & \text{Focal}(\text{Up}([M_n^l, M_a^l]), S_{\text{gt}}) \\ & + \text{Dice}(\text{Up}(M_n^l), I - S_{\text{gt}}) \\ & + \text{Dice}(\text{Up}(M_a^l), S_{\text{gt}}), \end{aligned} \quad (10)$$

where $[\cdot, \cdot]$ denotes channel-wise concatenation; for each layer l , M_n^l and M_a^l are the normal and anomaly score maps; S_{gt} is the ground-truth mask; and I is the all-ones matrix.

During inference, the final image-level anomaly score is computed as: Score = $\frac{1}{N} \sum_{l=1}^N S_a^l$. For pixel-level prediction, we merge all intermediate maps M_n^l and M_a^l , then obtain the anomaly map $\text{Map} \in \mathbb{R}^{H \times W}$ as follows:

$$\text{Map} = G_\sigma \left(\frac{1}{N} \sum_{l=1}^N \left(\frac{1}{2}(I - \text{Up}(M_n^l)) + \frac{1}{2} \text{Up}(M_a^l) \right) \right) \quad (11)$$

where G_σ denotes Gaussian smoothing.

5. Experiments

5.1. Setup

Datasets & Baselines To comprehensively evaluate ViP²-CLIP across diverse application scenarios, we conduct extensive experiments on public benchmarks spanning industrial and medical domains. In the industrial domain, we use MVTec AD [2], VisA [38], MPDD [15], BTAD [23], KSDD [30], DAGM [33], and DTD-Synthetic [1]. For medical imaging, we include brain tumour detection datasets HeadCT [29], BrainMRI [29], and Br35H [12], skin cancer detection dataset ISIC [7], colon polyp detection datasets CVC-ClinicDB [3], CVC-ColonDB [31], Endo [13], and Kvasir [16]. We compare ViP²-CLIP against six leading ZSAD methods: CLIP [26], WinCLIP [14], APRIL-GAN [5], AnomalyCLIP [37], AdaCLIP [4] and AA-CLIP [22]. Additional details regarding the datasets and methodological specifics are provided in Appendix B.

Metrics We adopt standard metrics for evaluation: for image-level anomaly detection, we report the Area Under the Receiver Operating Characteristic curve (AUROC), Average Precision (AP), and maximum F1 (F1); for pixel-level anomaly segmentation, we report AUROC, the Area Under the Per-Region Overlap curve (AUPRO), and F1.

Implementation Details We use the publicly released CLIP (ViT-L/14@336px) as the frozen backbone. The learnable prompts contain 10 tokens, 3 of which interact explicitly with the global visual embedding. In UTPA, we retain the top 50 anomalous patches at each alignment layer as image-level descriptors and, following prior work [4, 37], apply cross-modal alignment at layers 6, 12, 18, and 24. We fine-tune ViP²-CLIP on MVTec AD’s test split and evaluate ZSAD performance on all other datasets; for MVTec AD, we fine-tune on VisA’s test set. Dataset-level metrics are averaged across all subclasses. All experiments are implemented in PyTorch 2.6.0 on a single NVIDIA L20 (48 GB). Further implementation details are provided in Appendix B.

5.2. Main Results

Zero-Shot Anomaly Detection on Industrial Datasets Tab. 1 compares ViP²-CLIP against six representative baselines on seven industrial defect benchmarks. Our model delivers competitive results and outperforms all baselines in most datasets. The vanilla CLIP struggles, as its pre-training emphasizes general object semantics rather than anomaly patterns. WinCLIP and APRIL-GAN improve detection through handcrafted prompts and local features tuning. AnomalyCLIP employs object-agnostic prompts but remains limited by static prompt design and shallow cross-modal fusion. AA-CLIP directly introduces adapter modules to enlarge the semantic gap between normal and

Task	Datasets	C	CLIP	WinCLIP	APRIL-GAN	AnomalyCLIP	AdaCLIP	AA-CLIP	ViP ² -CLIP
			OpenCLIP	CVPR 2023	CVPRw 2023	ICLR 2024	ECCV 2024	CVPR 2025	-
Image-level (AUROC, AP, F1)	MVTec AD	15	(66.5, 82.6, 86.7)	(91.8, 96.5, 92.7) [*]	(86.1, 93.5, 90.4)	(91.6, 96.4, 92.7)	(90.1, 95.6, 92.3)	(89.1, 94.7, 90.0)	(91.2, 96.0, 92.0)
	VisA	12	(60.2, 66.2, 73.0)	(78.1, 81.2, 78.2) [*]	(77.5, 80.9, 78.7)	(82.0, 85.3, 80.4)	(87.2, 89.7, 83.5)	(78.9, 82.3, 78.8)	(88.5, 90.4, 84.8)
	MPDD	6	(58.7, 69.7, 76.0)	(61.5, 69.2, 77.5)	(76.8, 83.0, 81.0)	(77.5, 82.5, 80.4)	(74.8, 78.6, 83.3)	(56.9, 66.5, 74.5)	(79.7, 84.5, 82.4)
	KSDD	1	(74.3, 55.3, 57.8)	(92.4, 82.9, 77.7)	(96.5, 91.2, 85.4)	(97.8, 94.2, 89.7)	(97.2, 92.6, 89.5)	(96.0, 89.2, 84.7)	(98.1, 95.8, 93.2)
	BTAD	3	(25.7, 49.8, 66.0)	(68.2, 70.9, 67.8)	(73.7, 69.7, 68.2)	(88.2, 88.2, 83.8)	(89.3, 96.5, 90.9)	(93.4, 97.6, 93.9)	(95.0, 98.4, 94.7)
	DAGM	10	(55.3, 43.2, 49.6)	(91.8, 79.5, 75.7)	(94.4, 83.9, 80.2)	(97.7, 92.4 , 90.1)	(98.2, 92.3, 90.9)	(95.3, 87.5, 84.5)	(98.5, 94.3, 92.6)
	DTD-Synthetic	12	(52.3, 77.8, 85.1)	(95.1, 97.7, 94.1)	(85.6, 94.0, 89.1)	(93.9, 97.2, 93.6)	(96.3, 98.1, 95.5)	(94.0, 98.0, 94.3)	(95.5, 98.1, 94.3)
Pixel-level (AUROC, PRO, F1)	AVERAGE	-	(56.1, 63.5, 70.6)	(82.1, 82.1, 80.5)	(84.4, 85.2, 81.9)	(89.8, 90.9, 87.2)	(90.4, 91.9, 89.4)	(86.7, 88.0, 86.5)	(92.4, 93.9, 90.6)
	MVTec AD	15	(35.6, 10.6, 6.9)	(85.1, 64.6, 24.8) [*]	(87.6, 44.0, 43.3)	(91.1, 81.4, 39.1)	(89.6, 37.8, 45.1)	(91.5, 86.5, 46.7)	(90.5, 87.1 , 43.1)
	VisA	12	(43.6, 14.0, 1.5)	(79.6, 56.8, 9.0) [*]	(94.2, 86.6, 32.3)	(95.5, 86.7, 28.3)	(95.5, 56.8, 37.0)	(94.7, 82.7, 29.4)	(95.4, 92.2, 33.6)
	MPDD	6	(56.2, 27.3, 8.2)	(71.2, 40.5, 15.4)	(94.3, 83.8, 31.3)	(96.5, 88.7, 34.2)	(96.1, 60.3, 31.9)	(96.0, 86.6, 26.5)	(97.2, 92.6, 35.9)
	KSDD	1	(21.7, 2.6, 0.5)	(92.8, 70.3, 15.8)	(93.2, 84.1, 43.6)	(98.1, 94.9, 56.5)	(98.4, 53.0, 52.8)	(99.0, 92.2, 48.1)	(98.5, 96.2, 53.0)
	BTAD	3	(41.2, 10.8, 6.8)	(72.7, 27.5, 18.5)	(89.3, 68.7, 40.6)	(94.2, 75.4, 49.7)	(90.7, 22.3, 51.4)	(94.2, 70.0, 45.1)	(95.6, 86.1, 52.7)
	DAGM	10	(49.6, 12.4, 2.4)	(87.6, 65.7, 12.7)	(82.4, 66.0, 37.4)	(95.6, 91.0, 58.9)	(94.3, 42.5, 59.6)	(92.6, 79.7, 44.0)	(97.5, 95.2, 61.2)
Pixel-level (AUROC, PRO, F1)	DTD-Synthetic	12	(43.8, 16.0, 3.7)	(79.5, 51.4, 16.1)	(95.2, 87.3, 67.4)	(97.9, 92.0, 62.2)	(98.5, 75.0, 71.8)	(97.4, 88.9, 58.0)	(99.0, 96.5, 67.5)
	AVERAGE	-	(47.1, 13.4, 4.3)	(79.9, 52.6, 16.0)	(90.9, 74.4, 42.2)	(95.6, 87.2, 47.0)	(94.7, 49.7, 49.9)	(95.0, 83.8, 42.5)	(96.2, 92.3, 49.6)

Table 1. ZSAD performance comparison on industrial domain. ^{*} denotes results taken from original papers. The best performance is shown in red, with the second-best highlighted in blue.

Task	Datasets	C	CLIP	WinCLIP	APRIL-GAN	AnomalyCLIP	AdaCLIP	AA-CLIP	ViP ² -CLIP
			OpenCLIP	CVPR 2023	CVPRw 2023	ICLR 2024	ECCV 2024	CVPR 2025	-
Image-level (AUROC, AP, F1)	HeadCT	1	(67.8, 62.4, 70.9)	(81.8, 80.2, 78.9)	(89.1, 89.4, 82.1)	(93.0, 91.1, 88.4)	(94.0, 91.4, 90.1)	(88.1, 90.4, 80.6)	(94.3, 93.9, 88.1)
	BrainMRI	1	(72.2, 81.5, 76.5)	(86.6, 91.5, 84.1)	(89.4, 91.0, 88.2)	(90.0, 92.1, 86.5)	(94.3, 95.5, 92.2)	(92.2, 94.5, 88.6)	(95.3, 96.7, 92.3)
	Brain35H	1	(76.3, 77.7, 72.2)	(79.9, 82.2, 74.0)	(91.6, 92.1, 84.5)	(93.4, 93.8, 86.4)	(95.7, 95.8, 91.1)	(89.3, 90.6, 81.6)	(95.8, 96.0, 90.1)
	AVERAGE	-	(72.1, 73.9, 73.2)	(82.8, 84.6, 79.0)	(90.0, 90.8, 84.9)	(92.1, 92.3, 87.1)	(94.7, 94.2, 91.1)	(89.9, 91.8, 83.6)	(95.1, 95.5, 90.2)
Pixel-level (AUROC, PRO, F1)	ISIC	1	(43.2, 7.6, 44.0)	(83.3, 55.1, 64.1)	(89.4, 77.2, 71.4)	(89.4, 78.4, 71.6)	(91.3, 53.2, 75.5)	(91.6, 86.2, 78.1)	(90.3, 82.3 , 73.7)
	CVC-ColonDB	1	(59.8, 30.4, 17.8)	(64.8, 28.4, 21.0)	(78.4, 64.6, 29.7)	(81.9, 71.2, 37.5)	(81.5, 64.3, 33.6)	(80.6, 62.1, 32.3)	(82.5, 74.8, 36.2)
	CVC-ClinicDB	1	(63.1, 33.8, 23.4)	(70.3, 32.5, 27.2)	(80.5, 60.7, 38.7)	(82.9, 68.1, 42.4)	(83.9, 65.7, 42.3)	(85.6, 66.3, 44.3)	(86.3, 72.1, 44.9)
	Endo	1	(59.7, 25.2, 28.9)	(68.2, 28.3, 32.9)	(81.9, 54.9, 44.8)	(84.2, 63.4, 50.3)	(86.0, 63.4, 51.8)	(86.0, 66.5, 54.0)	(84.5, 63.7, 49.2)
	Kvasir	1	(58.0, 18.3, 29.3)	(69.7, 24.5, 35.9)	(75.0, 36.3, 40.0)	(79.0, 45.4, 46.2)	(81.6, 49.1, 47.1)	(81.5, 48.4, 49.2)	(81.9, 47.8, 47.3)
	AVERAGE	-	(56.8, 23.1, 28.7)	(71.3, 33.8, 36.2)	(81.0, 58.7, 44.9)	(83.5, 65.3, 49.6)	(84.9, 59.1, 50.1)	(85.1, 65.9, 51.6)	(85.1, 68.1, 50.3)

Table 2. ZSAD performance comparison on medical domain. The best performance is shown in red, with the second-best highlighted in blue. Note that the image-level medical AD datasets do not provide pixel-level segmentation annotations, so the pixel-level medical AD datasets are different from the image-level datasets.

anomalous texts, thereby enhancing detection performance. AdaCLIP refines prompts in both visual and textual space, which boosts F1 but neglects AUPRO, leading to an imbalanced ZSAD. In contrast, ViP²-CLIP yields consistent improvements across all metrics, achieving state-of-the-art performance. Our ViP-Prompt creates fine-grained normal and abnormal prompts that align tightly with object features; paired with UTPA’s unified alignment strategy, substantially improves overall ZSAD performance. Fig. 4 further compares the anomaly detection results of our approach with five strong baselines, showing that ViP²-CLIP more accurately captures defects with sharper boundaries, supporting the observed quantitative gains. We also provide failure-case analyses in Appendix C.

Zero-Shot Anomaly Detection on Medical Datasets To assess cross-domain transferability, we benchmark ViP²-CLIP on eight public medical defect datasets. As shown in Tab. 2, although AA-CLIP achieves stronger pixel-level anomaly localization, its weaker image-level detection results in unbalanced ZSAD performance. In contrast, our ViP²-CLIP consistently delivers superior results across most datasets. Qualitative examples in Fig. 4 also support this claim: our model precisely localizes melanoma

lesions in dermoscopy images and colonic polyps in endoscopic frames, demonstrating robust adaptability to disparate pathological patterns.

Static prompts vs. Visual-Perception prompts To quantify the benefit of visual conditioning, we compare ViP²-CLIP against ViP²-CLIP_{re}, which only uses static learnable prompts without visual cues. Fig. 5 reports image-level and pixel-level F1 gains on the seven industrial datasets. ViP²-CLIP achieves higher pixel-level F1 on all datasets and improves image-level F1 on five of them. The slight drops on BTAD and DAGM are attributed to significant domain shifts from MVTec AD: BTAD reflects real-world industrial settings with complex lighting conditions, while DAGM contains synthetic textures characterized by small, repetitive anomalies. Such shifts likely distort global visual embeddings, reducing the transferability of ICA and resulting in imbalanced performance. Despite minor image-level declines on a few datasets, ViP-Prompt consistently achieves SOTA performance across diverse detection scenarios. It effectively mitigates segmentation fluctuations arising from uncertain class names in prompts under data privacy constraints (as detailed in Appendix A), thereby ensuring more robust generalization.

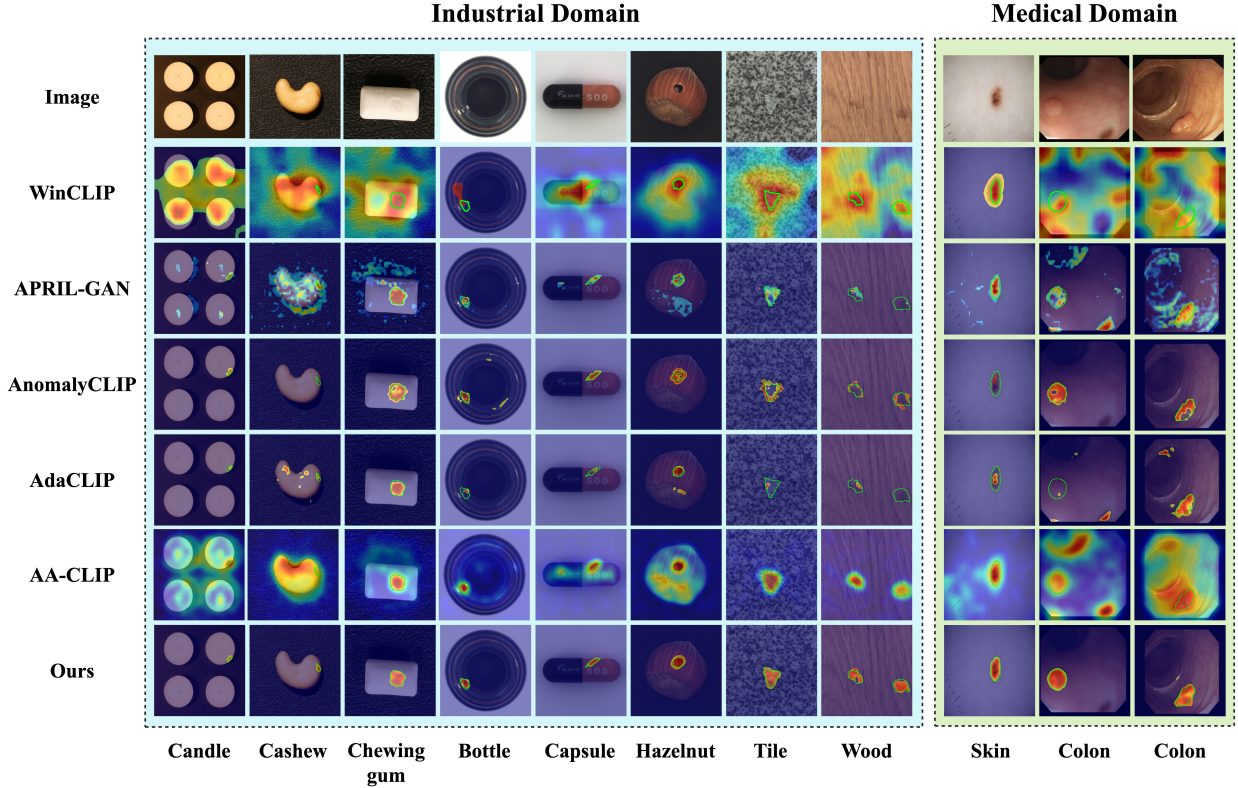


Figure 4. Visualization of anomaly maps of different ZSAD methods. Our proposed ViP²-CLIP achieves the sharpest segmentations, capturing fine-grained defects in both industrial and medical datasets.

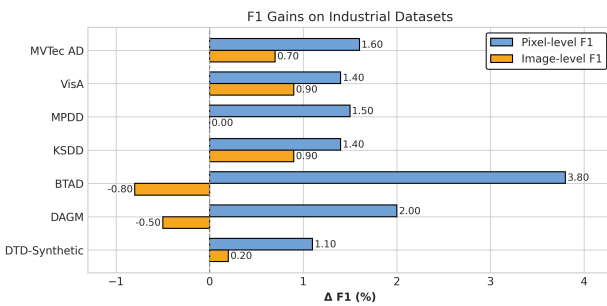


Figure 5. F1 gains of using visual-conditioned prompts compared to static learnable prompts.

Computational Efficiency Analysis Tab. 3 compares the computational efficiency with the top three baselines. AnomalyCLIP modifies self-attention weights via DPAM, while AdaCLIP introduces additional learnable tokens and a multi-scale clustering module, both of which increase computational overhead. Although AA-CLIP attains the shortest inference time through a simplified network design, its large number of trainable parameters diminishes overall efficiency. In contrast, ViP²-CLIP employs only two

Model	Training Time (h)	Inference Time (ms)	GPU Cost (GB)	Trainable Parameters (M)
AnomalyCLIP	1.02	90.72 ± 0.16	2.75	5.56
AdaCLIP	2.24	134.20 ± 0.39	3.17	10.67
AA-CLIP	0.93	19.17 ± 0.23	2.87	12.58
Ours	0.54	48.69 ± 0.19	2.21	4.15

Table 3. Comparison of computational efficiency on VisA.

lightweight adapters outside the frozen CLIP backbone, enabling the fastest training (0.54 h), competitive inference speed (48.7 ms/image), and the lowest GPU memory consumption (2.21 GB), making it highly suitable for deployment in resource-constrained industrial environments.

5.3. Ablation Study & Discussion

Module Ablation We isolate the contributions of three key components: ViP-ICA, ViP-FGP, and UTPA. Tab. 4 shows that adding each module yields a clear, consistent gain, validating their standalone effectiveness. Specifically, ICA adaptively injects global visual context into prompt embeddings, while FGP incorporates fine-grained local cues, enabling the prompts to capture precise irregularities. Furthermore, UTPA consistently improves both detection and localization performance upon integration, demonstrating the general effectiveness of the unified patch-

UTPA	ViP-Prompt	MVTec AD				VisA	
		ICA	FGP	Pixel-level	Image-level		
		(37.8, 11.5, 7.0)		(74.1, 87.6, 87.2)		(43.5, 14.6, 2.8)	(60.2, 66.3, 74.5)
✓		(89.5, 79.9, 38.6)		(71.8, 86.2, 88.5)		(95.2, 90.9, 31.6)	(79.7, 82.8, 79.5)
	✓	(90.0, 85.5, 42.7)		(66.1, 82.6, 86.6)		(95.3, 91.5, 33.4)	(60.1, 66.4, 73.5)
✓	✓	(87.7, 83.8, 42.4)		(88.9, 94.9, 91.6)		(95.2, 91.6, 35.5)	(83.0, 85.9, 81.4)
✓	✓	(89.8, 84.4, 40.2)		(89.2, 95.0, 91.4)		(94.9, 91.4, 31.3)	(86.3, 89.1, 83.8)
✓	✓	(88.8, 82.1, 38.7)		(85.2, 93.3, 89.0)		(95.3, 91.9, 31.4)	(87.6, 89.4, 83.8)
✓	✓	(90.5, 87.1, 43.1)		(91.2, 96.0, 92.0)		(95.4, 92.2, 33.6)	(88.5, 90.4, 84.8)

Table 4. Module ablation.

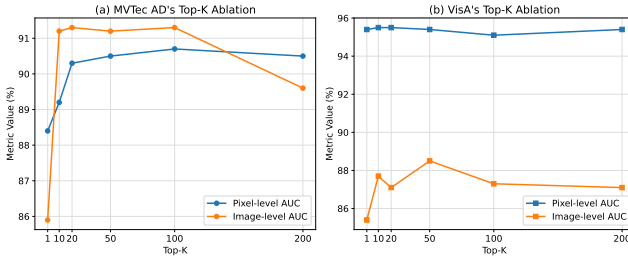


Figure 6. Top-k component ablation.

level alignment strategy in guiding prompt learning toward more discriminative representations.

UTPA for Resolving Optimization Conflicts We conduct an ablation study using a frozen CLIP backbone with learnable prompts for normal and anomalous classes to evaluate the effectiveness of UTPA in guiding model learning. The baseline (CLIP_DUAL) adopts a dual-branch strategy that aligns prompts with both global and local visual cues. In contrast, CLIP_UTPA simplifies the optimization by aligning solely with local features. As shown in Tab. 13, on the MVTec AD dataset, the dual-branch strategy tends to overfit image-level scores while underperforming on pixel-level detection. UTPA, by comparison, achieves more stable and superior results. As for VisA, it outperforms the baseline across both detection metrics. Several results in Tab. 4 also support this observation: traditional dual-branch approaches often suffer from imbalanced performance due to conflicting objectives, whereas UTPA alleviates this issue through consistent text-patch alignment. This facilitates more robust model learning and provides a novel alignment paradigm for more accurate ZSAD research.

Top-K Ablation To assess how the image-level representation is affected by the number of anomalous patches, we vary $K \in \{1, 10, 20, 50, 100, 200\}$ and examine the AUROC performance in Fig. 6. At $K = 1$, the model is overly sensitive to local noise, yielding a low AUROC. As K increases, performance steadily improves, demonstrating that aggregating multiple high-scoring anomalous patches enhances robustness. On MVTec AD, performance plateaus when K is at 50 or 100; As for VisA, the optimum occurs at $K = 50$. Beyond these points, additional patches introduce mostly normal regions, diluting the anomaly sig-

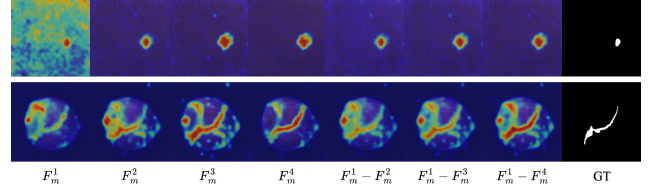


Figure 7. Visualization of anomaly maps from different layers.

Module	MVTec AD		VisA	
	Pixel-level	Image-level	Pixel-level	Image-level
CLIP_DUAL	(69.6, 24.6, 12.0)	(88.6, 94.9, 91.3)	(93.3, 82.4, 24.2)	(79.3, 82.4, 79.0)
CLIP_UTPA	(89.6, 83.7, 37.4)	(85.0, 93.3, 88.8)	(94.4, 88.4, 26.2)	(83.8, 86.7, 81.4)

Table 5. Ablation on the effectiveness of UTPA.

nals and reducing accuracy. Balanced across all metrics, we select the top 50 most anomalous patches as image-level descriptors, which effectively capture the anomaly characteristics in most detection scenarios.

Visualization at Different layers To examine the impact of model depth on anomaly representation, Fig. 7 presents anomaly maps derived from F_m^1 to F_m^4 layers. For complex object categories such as hazelnut, deeper layers yield more accurate anomaly localization. In contrast, for simpler texture-based objects like leather, intermediate layers offer sufficient discriminative power. Aggregating features across multiple depths provides complementary contextual cues, allowing the model to better adapt to diverse anomaly types, and thereby achieve more robust anomaly detection.

6. Conclusion

We propose ViP²-CLIP, a universal ZSAD framework that detects anomalies in unseen categories without any target domain training samples. At its core, ViP-Prompt adaptively integrates global and local visual cues into text prompts, eliminating reliance on manual templates or class-name priors, achieving superior generalization and robustness in cross-modal alignment. In addition, the UTPA optimizes a unified text-patch alignment strategy across scales, sharpening both detection and localization performance. Extensive experiments on 15 mainstream datasets demonstrate that ViP²-CLIP consistently outperforms existing methods across various detection scenarios, especially when category labels are ambiguous or privacy-constrained, offering a more accurate and scalable solution for ZSAD.

Limitations Although UTPA achieves high-precision ZSAD performance through a simple yet effective alignment strategy, its current implementation only selects the better-performing Top-K from a small set of discrete candidates, further work on more advanced feature aggregation strategies is needed to explore.

A. Motivation Statement

A.1. Robustness Analysis of Class-Name in Prompts

Methods like CLIP-AD [6], AdaCLIP [4], and KANOCLIP [19] enhance alignment by embedding class names into prompts, but this introduces a critical vulnerability: CLIP’s segmentation quality is highly sensitive to label phrasing. Specifically, we conducted synonym-swap experiments on the training-free WinCLIP model to evaluate how CLIP’s inherent segmentation capability is influenced by the class-name variations. As shown in Fig. 8, by replacing class names with semantically equivalent variants (e.g., ‘zipper’ to ‘zip’ or ‘fastener’), we observed a striking inconsistency: pixel-level segmentation metrics can vary by up to 10 percentage points, while image-level classification metrics remain stable. We attribute this instability to CLIP’s classification-oriented pre-training, which enforces robust global alignment but yields fragile local alignment.

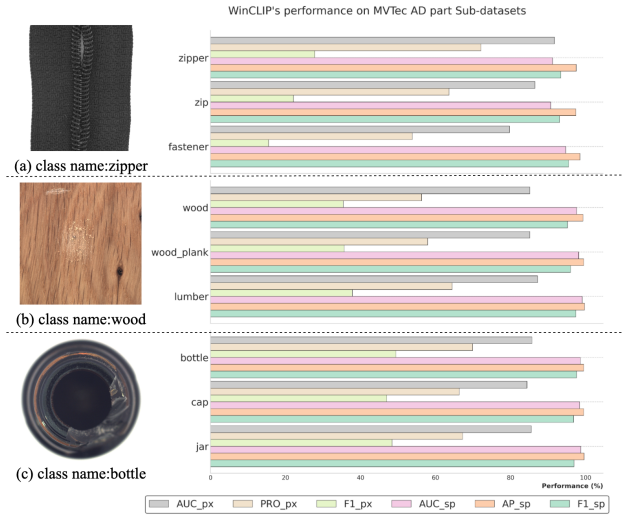


Figure 8. WinCLIP’s performance of different Class Names in Prompts.

To further evaluate whether training-based modality alignment can alleviate this sensitivity, we repeated the synonym-swap experiments on recent work, AdaCLIP. As shown in Fig. 9, although AdaCLIP’s pixel-level F1 stays stable, its AUROC and PRO fluctuate with label swaps; in particular, changing ‘carpet’ to ‘floor mat’ triggers a 47% swing in PRO. This dramatic fluctuation shows that, even with fine-tuning on auxiliary data, the limited scale of anomaly-specific training cannot effectively mitigate CLIP’s segmentation sensitivity to class-name perturbations. These findings underscore the necessity of label-agnostic prompt designs for truly robust ZSAD.

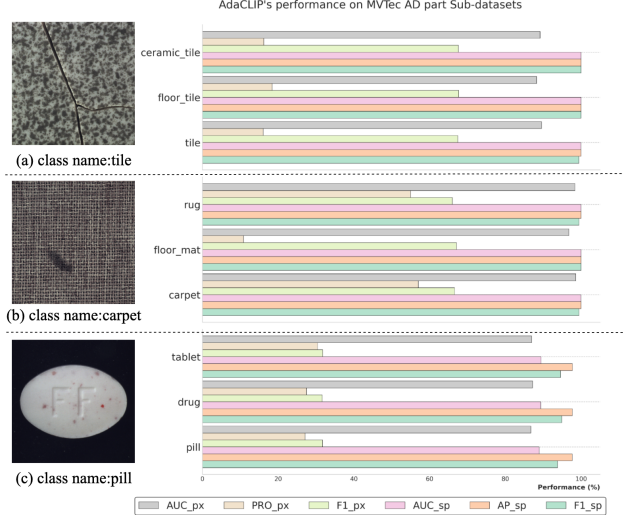


Figure 9. AdaCLIP’s performance of different Class Names in Prompts.

B. Experimental Details

B.1. Implementation Details

We use the publicly released CLIP (ViT-L/14@336px) model as the frozen feature extractor. In all experiments, the learnable prompt length is set to 10, of which 3 tokens fuse with the global visual feature. In UTPA, we set $Top-k = 50$ and perform cross-modal alignment at layers $\{6, 12, 18, 24\}$. During training, input images are resized to 518×518 , we optimize with Adam at a learning rate of 1×10^{-3} for 10 epochs with a batch size of 8. All experiments are implemented in PyTorch 2.6.0 on a single NVIDIA L20 (48 GB).

We conduct comprehensive evaluations across 15 publicly available benchmarks spanning industrial and medical domains. Specifically, we fine-tune on MVTec AD’s test set and perform zero-shot evaluation on all other datasets; for MVTec AD, we fine-tune on VisA’s test split. We adopt standard metrics for evaluation: Area Under the ROC Curve (AUC), Average Precision (AP), and F1-score (F1) for image-level anomaly detection; AUC, Per-Region Overlap (PRO), and F1 for pixel-level segmentation.

B.2. Baselines

To validate the superiority of ViP²-CLIP, we compare against the following state-of-the-art methods:

- **CLIP** [26]: We adapt CLIP for anomaly detection by using two prompt templates—‘a photo of a normal [cls]’ and ‘a photo of an abnormal [cls]’, where [cls] is the category class-name. We compute image-level anomaly scores via cosine similarity between global visual features and text embeddings. For pixel-level segmentation, we

Domain	Dataset	Category	Modalities	$ \mathcal{C} $	Normal and anomalous samples
Industrial	MVTec AD	Obj	Photography	15	(467, 1258)
	VisA		Photography	12	(962, 1200)
	MPDD		Photography	6	(176, 282)
	BTAD		Photography	3	(451, 290)
	KSDD		Photography	1	(286, 54)
	DAGM	Texture	Photography	10	(6996, 1054)
	DTD-Synthetic		Photography	12	(357, 947)
Medical	ISIC	Skin	Photography	1	(0, 379)
	CVC-ClinicDB	Colon	Endoscopy	1	(0, 612)
	CVC-ColonDB		Endoscopy	1	(0, 380)
	Kvasir		Endoscopy	1	(0, 1000)
	Endo		Endoscopy	1	(0, 200)
	HeadCT	Brain	Radiology (CT)	1	(100, 100)
	BrainMRI		Radiology (MRI)	1	(98, 155)
	Br35H		Radiology (MRI)	1	(1500, 1500)

Table 6. Statistics of the datasets.

extend this scoring to the last-layer patch embeddings.

- **WinCLIP** [14]: WinCLIP is the first CLIP-based ZSAD method, which uses multiple manually designed prompts and a multi-window feature extraction strategy. All parameters are kept the same as in their paper.
- **APRIL-GAN**[5]: APRIL-GAN extends WinCLIP by incorporating learnable linear projection layers to enrich local visual feature representations. All experiments are conducted using the official weights and adhere strictly to the original implementation protocols.
- **AnomalyCLIP** [37]: AnomalyCLIP introduces object-agnostic learnable prompts and a DPAM mechanism for stronger local features’ modelling. All experiments are conducted using publicly released official model weights.
- **AdaCLIP** [4]: AdaCLIP incorporates hybrid prompts into both text and image encoders with an HSF module for improved cross-modal fusion. As AdaCLIP adopts an evaluation protocol distinct from ours, it trains on MVTec AD and CVC-ColonDB and performs zero-shot testing on the remaining datasets. To ensure fair and consistent comparison, we reimplement AdaCLIP under our unified evaluation protocol. All parameters are kept the same as in their paper.
- **AA-CLIP** [22]: AA-CLIP enhances anomaly detection by adopting a two-stage training strategy that enlarges the semantic gap between normal and anomalous texts through joint optimization of the text and image encoders. We reimplement it under our unified evaluation protocol, keeping all parameters consistent with the original paper.

B.3. Datasets

We evaluate on 7 industrial datasets (MVTec AD, VisA, MPDD, BTAD, KSDD, DAGM, DTD-Synthetic) and 8 medical datasets (HeadCT, BrainMRI, Br35H, ISIC, CVC-ClinicDB, CVC-ColonDB, Endo, Kvasir), for a total of 15 benchmarks. All methods are trained and tested solely on each dataset’s test split. The dataset statistics are given in Tab. 6. We apply OpenCLIP’s default normalization to all images and resize them to (518, 518) to obtain suitably scaled feature maps.

C. Additional Experiments and Analysis

C.1. Comparison with Full-shot Methods

In this section, we compare ViP²-CLIP against two state-of-the-art full-shot methods, PatchCore [28] and RD4AD [8], on five industrial datasets for which training samples are available. Results are presented in Tab. 7. Despite not using any target domain training samples, ViP²-CLIP achieves detection and segmentation performance on par with or superior to these fully supervised approaches, with particularly strong gains on the BTAD and DAGM datasets. This demonstrates that ViP²-CLIP’s visual-perception prompt mechanism adaptively generates fine-grained normal and anomalous text descriptions that fully unleash CLIP’s ZSAD performance, breaking the dependency of traditional methods on in-domain training data and exhibits excellent generalization.

Task	Category	Datasets	PatchCore*	RD4AD*	ViP ² -CLIP
Image-level (AUROC, AP)	Obj &texture	MVTec AD	(99.0, 99.7)	(98.7, 99.4)	(91.2, 96.0)
		VisA	(94.6, 95.9)	(95.3, 95.7)	(88.5, 90.4)
		Obj	(94.1, 96.3)	(91.6, 93.8)	(79.7, 84.5)
			(93.2, 98.6)	(93.8, 96.8)	(95.0, 98.4)
	Texture	DAGM	(92.7, 81.3)	(92.9, 79.1)	(98.5, 94.3)
	Pixel-level (AUROC, PRO)	Obj &texture	(98.1, 92.8)	(97.8, 93.6)	(90.5, 87.1)
			(98.5, 92.2)	(98.4, 91.2)	(95.4, 92.2)
		Obj	(98.8, 94.9)	(98.4, 95.2)	(97.2, 92.6)
			(97.4, 74.4)	(97.5, 75.1)	(95.6, 86.1)
		Texture	(95.9, 87.9)	(96.8, 91.9)	(97.5, 95.2)

Table 7. Comparison of ZSAD performance between ViP²-CLIP and SOTA full-shot methods. Results of methods with * are copied from the AnomalyCLIP paper. The best performance is highlighted in red, and the second is highlighted in blue.

Task	Datasets	$ C $	AnomalyCLIP	ViP ² -CLIP
Image-level (AUROC, AP, F1)	HeadCT	1	(94.3, 94.0, 90.5)	(96.5, 96.5, 92.8)
	BrainMRI	1	(94.7, 95.7, 92.5)	(96.7, 97.6, 94.9)
	Brain35H	1	(96.5, 96.7, 92.6)	(97.1, 97.5, 93.4)
	AVERAGE	-	(95.2, 95.5, 91.9)	(96.8, 97.2, 93.7)
Pixel-level (AUROC, PRO, F1)	ISIC	1	(87.8, 75.6, 69.7)	(91.7, 82.9, 75.3)
	CVC-ColonDB	1	(87.8, 76.9, 48.5)	(87.7, 86.2, 53.5)
	CVC-ClinicDB	1	(88.8, 76.1, 51.7)	(92.2, 84.3, 60.8)
	Endo	1	(89.0, 73.5, 58.1)	(92.3, 82.8, 65.2)
	Kvasir	1	(85.6, 50.0, 55.1)	(90.5, 56.9, 63.4)
	AVERAGE	-	(87.8, 70.4, 56.6)	(90.9, 78.6, 63.6)

Table 8. ZSAD performance on medical images after fine-tuning by medical-domain datasets. Best performance is shown in red.

C.2. Targeted Fine-tuning on Medical Data

Although ViP²-CLIP achieves strong results on industrial benchmarks, its performance on medical images is relatively weaker, partly due to the domain gap between industrial data and medical target domains. To investigate whether fine-tuning on medical auxiliary data can bridge this gap, we design a cross-domain fine-tuning protocol: we train on MVTec AD and CVC-ColonDB test split and test on the remaining medical datasets; for CVC-ColonDB, we use VisA and CVC-ClinicDB test sets as auxiliary data. We compare against AnomalyCLIP under the same training strategy. As shown in Tab. 8, introducing medical auxiliary data significantly boosts detection performance, particularly on CVC-ClinicDB and Endo datasets, highlighting the critical role of auxiliary data in cross-domain generalization. Overall, ViP²-CLIP outperforms AnomalyCLIP under medical fine-tuning, demonstrating superior cross-domain anomaly detection capability.

C.3. State-Adjective Ablation

To verify our prompt’s robustness, we replace the original ‘good/damaged’ adjectives with several alternative pairs

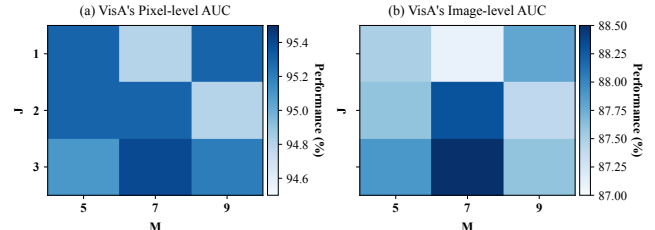


Figure 10. Prompt Length ablation.

State words	MVTec AD		VisA	
	Pixel-level	Image-level	Pixel-level	Image-level
Good/Damage	(90.5, 87.1, 43.1)	(91.2, 96.0, 92.0)	(95.4, 92.2, 33.6)	(88.5, 90.4, 84.8)
Normal/Abnormal	(90.6, 87.5, 43.6)	(91.1, 95.9, 92.3)	(95.3, 91.9, 33.3)	(88.3, 90.2, 84.5)
Perfect/Flawed	(90.4, 87.2, 43.7)	(91.7, 96.2, 92.5)	(95.4, 92.0, 33.5)	(88.3, 90.3, 84.5)
Flawless/Imperfect	(90.4, 87.4, 43.3)	(91.2, 95.9, 92.2)	(95.4, 91.9, 33.1)	(87.9, 90.2, 84.3)

Table 9. Ablation on different state words in prompts.

of similar meaning and retrain the model on MVTec-AD and VisA. As Tab. 9 shows, detection performance remains consistent across all variants, demonstrating insensitivity to specific adjective choices. This resilience stems from our learnable prompt tokens, which autonomously capture normal and anomalous semantics, obviating the need for hand-crafted text templates.

C.4. Prompt Length Ablation

Next, based on VisA dataset, we vary the total prompt length to assess its effect on ZSAD performance, focusing on both the number of static learnable tokens M and dynamic tokens J , which fuse with global visual context. Fig. 10 shows that increasing length does not always improve performance: too many learnable tokens introduce redundancy and risk overfitting, harming precision and generalization capacity. To balance between semantic expres-

siveness and model robustness, we set the prompt length to 10 by default, comprising 3 dynamic tokens infused with global visual semantics and 7 static tokens modelling generic normal and anomalous patterns.

C.5. Failure Cases

ViP²-CLIP performs well in clean and controlled environments with localized anomalies, but certain failure cases arise in more complex scenarios:

Contextual Anomalies The model struggles to detect contextual anomalies—such as abnormal spatial arrangements or misaligned components—that lack explicit visual distortions. These cases remain challenging without prior knowledge of normal structural configurations. This highlights a promising direction: integrating object-level positional priors or spatial layout descriptions into prompt design to enhance contextual reasoning.

Highly Textured Backgrounds Our method assumes that the target object is centrally located within a clean background, allowing the image encoder to extract a reliable global visual embedding for prompt generation. However, in cluttered scenes or when multiple objects are present, the quality of the extracted global embedding deteriorates. The absence of class name guidance further impairs localization, reducing detection accuracy.

Uneven Anomaly Distributions In UTPA, a fixed Top-K patch aggregation strategy is used to represent global anomaly features. However, when anomalies are unevenly distributed across the image, the choice of K affects performance. While our Top-50 selection achieves SOTA results under the detection settings of most datasets, future work should explore adaptive aggregation mechanisms to better accommodate varying anomaly distributions.

D. Additional Quantitative and Qualitative Results

D.1. Fine-grained Subset Performance

Tab. 10–Tab. 21 report detailed ZSAD performance at the subset level on MVTec AD and VisA datasets, illustrating ViP²-CLIP’s ability to handle fine-grained variations within each category.

D.2. Visualization

We visualize pixel-wise anomaly maps in Fig. 11–Fig. 22, demonstrating ViP²-CLIP’s strong segmentation capability and cross-domain generalization. Industrial examples include capsule, grid, leather, screw and hazelnut from MVTec AD; candle, cashew, macaroni, pcb and pipe fryum

from VisA; brackets and metal plates from MPDD; and unknown products from BTAD. Medical examples cover melanoma detection in ISIC, and colorectal polyp detection in CVC-ColonDB and CVC-ClinicDB.

Object name	CLIP	WinCLIP	APRIL-GAN	AdaCLIP	AnomalyCLIP	ViP ² -CLIP
Candle	32.7	87.0	97.8	98.9	98.8	99.0
Capsules	44.8	80.0	97.5	98.7	95.0	98.3
Cashew	21.8	84.8	85.8	92.1	93.8	91.4
Chewinggum	37.8	95.4	99.5	99.6	99.3	99.7
Fryum	26.0	87.7	91.9	94.5	94.6	92.6
Macaroni1	52.9	50.3	98.8	99.2	98.3	99.5
Macaroni2	70.4	44.7	97.8	98.4	97.6	98.7
Pcb1	61.9	38.6	92.8	93.7	94.0	90.1
Pcb2	27.4	58.7	89.8	90.8	92.4	92.0
Pcb3	71.7	76.0	88.2	88.5	88.4	92.2
Pcb4	49.2	91.4	94.5	96.1	95.7	96.4
Pipe_fryum	26.9	83.6	96.0	96.0	98.2	95.2
Mean	43.6	73.2	94.2	95.5	95.5	95.4

Table 10. Fine-grained performance comparison for Pixel-level AUROC on VisA.

Object name	CLIP	WinCLIP	APRIL-GAN	AnomalyCLIP	AdaCLIP	ViP ² -CLIP
Candle	7.9	77.7	92.3	96.5	62.2	96.7
Capsules	12.0	39.4	86.1	78.9	38.3	93.5
Cashew	0.3	78.4	91.5	91.9	57.5	94.9
Chewinggum	9.1	69.6	87.5	90.9	55.8	96.8
Fryum	6.1	74.4	89.4	86.9	52.7	94.8
Macaroni1	25.9	24.8	93.0	89.8	65.6	96.4
Macaroni2	32.6	8.0	82.0	84.0	62.9	89.5
Pcb1	18.4	20.7	87.3	80.7	47.7	91.4
Pcb2	8.2	20.7	75.4	78.9	50.2	80.0
Pcb3	27.2	43.8	77.2	76.8	41.8	84.3
Pcb4	11.6	74.5	86.6	89.4	63.9	90.7
Pipe_fryum	9.1	80.3	90.9	96.2	83.2	97.2
Mean	14.0	51.0	86.6	86.7	56.8	92.2

Table 11. Fine-grained performance comparison for Pixel-level AUPRO on VisA.

Object name	CLIP	WinCLIP	APRIL-GAN	AnomalyCLIP	AdaCLIP	ViP ² -CLIP
Candle	0.3	8.9	39.4	37.8	42.1	42.4
Capsules	1.1	4.2	49.1	37.8	54.1	50.7
Cashew	2.2	9.6	22.7	25.8	35.1	23.8
Chewinggum	1.1	31.6	78.5	61.0	78.2	74.4
Fryum	4.5	16.2	29.5	30.3	32.7	25.6
Macaroni1	0.1	0.1	35.3	23.7	32.7	38.9
Macaroni2	0.1	0.1	13.9	5.1	14.1	9.7
Pcb1	2.3	0.9	12.2	12.7	13.7	13.4
Pcb2	0.4	1.5	23.3	15.8	32.5	23.4
Pcb3	1.2	2.1	21.9	9.3	35.8	25.7
Pcb4	1.5	24.6	31.0	34.7	43.0	39.8
Pipe_fryum	2.5	8.3	30.4	45.5	29.5	35.9
Mean	1.5	9.0	32.3	28.3	37.0	33.6

Table 12. Fine-grained performance comparison for Pixel-level F1 on VisA.

Object name	CLIP	WinCLIP	APRIL-GAN	AnomalyCLIP	AdaCLIP	ViP ² -CLIP
Candle	55.2	94.8	82.6	80.9	96.0	90.4
Capsules	61.9	79.4	62.3	82.8	87.0	93.8
Cashew	68.3	91.2	86.6	76.0	88.1	96.4
Chewinggum	59.4	95.5	96.4	97.2	93.9	97.9
Fryum	48.4	73.6	93.8	92.7	91.8	88.5
Macaroni1	61.5	79.0	69.3	86.7	84.2	86.3
Macaroni2	52.3	67.1	65.7	72.2	67.5	70.8
Pcb1	66.1	72.1	51.0	85.2	89.2	90.8
Pcb2	64.4	47.0	71.4	62.0	84.3	78.8
Pcb3	50.7	63.9	66.9	61.7	78.9	78.3
Pcb4	64.8	74.2	94.7	93.9	95.3	97.5
Pipe_fryum	68.9	67.9	89.2	92.3	90.3	92.4
Mean	60.2	75.5	77.5	82.0	87.2	88.5

Table 13. Fine-grained performance comparison for Image-level AUROC on VisA.

Object name	CLIP	WinCLIP	APRIL-GAN	AnomalyCLIP	AdaCLIP	ViP ² -CLIP
Candle	56.1	95.4	86.0	82.6	96.6	92.6
Capsules	74.9	87.9	74.5	89.4	92.5	96.7
Cashew	80.9	96.0	93.8	89.3	94.9	98.4
Chewinggum	77.3	98.2	98.4	98.8	97.5	99.1
Fryum	70.4	86.9	97.1	96.6	96.3	94.5
Macaroni1	60.3	80.0	67.4	85.5	83.1	87.9
Macaroni2	49.9	65.1	64.8	70.8	67.7	71.1
Pcb1	69.9	73.0	55.3	86.7	89.4	91.0
Pcb2	62.5	46.1	73.4	64.4	85.6	78.9
Pcb3	50.6	63.1	70.4	69.4	82.4	81.6
Pcb4	59.6	70.1	94.8	94.3	95.5	96.8
Pipe_fryum	82.1	82.1	94.5	96.3	95.1	96.3
Mean	66.2	78.7	80.9	85.3	89.7	90.4

Table 14. Fine-grained performance comparison for Image-level AP on VisA.

Object name	CLIP	WinCLIP	APRIL-GAN	AnomalyCLIP	AdaCLIP	ViP ² -CLIP
Candle	67.4	90.6	77.9	75.6	89.5	83.0
Capsules	76.9	80.5	78.0	82.2	85.0	90.8
Cashew	80.2	88.9	85.4	80.3	86.8	94.0
Chewinggum	80.0	93.8	93.2	94.8	91.5	96.4
Fryum	80.0	80.0	91.5	90.1	88.2	88.2
Macaroni1	71.5	74.2	70.8	80.4	80.4	79.6
Macaroni2	66.7	68.8	69.3	71.2	68.8	71.3
Pcb1	68.1	70.2	66.9	78.8	81.5	85.0
Pcb2	68.4	67.1	69.1	67.8	77.5	74.1
Pcb3	66.4	67.6	66.7	66.4	73.6	73.3
Pcb4	69.6	75.7	87.3	87.8	89.7	92.4
Pipe_fryum	80.8	80.3	88.1	89.8	89.0	89.5
Mean	73.0	78.2	78.7	80.4	83.5	84.8

Table 15. Fine-grained performance comparison for Image-level F1 on VisA.

Object name	CLIP	WinCLIP	VAND	AnomalyCLIP	AdaCLIP	ViP ² -CLIP
Carpet	18.0	90.9	98.4	98.8	98.6	99.2
Bottle	19.6	85.7	83.5	90.4	92.8	89.4
Hazelnut	27.6	95.7	96.1	97.2	98.6	96.7
Leather	12.7	95.5	99.1	98.6	99.3	99.2
Cable	44.1	61.3	72.3	78.9	76.6	73.2
Capsule	58.0	87.0	92.0	95.8	94.3	94.4
Grid	11.8	79.4	95.8	97.3	91.1	97.7
Pill	45.6	72.7	76.2	91.8	86.7	87.5
Transistor	42.2	83.7	62.4	70.8	63.5	64.6
Metal Nut	33.3	49.3	65.5	74.6	68.2	76.8
Screw	72.3	91.1	97.8	97.5	97.8	98.7
Toothbrush	26.0	86.2	95.8	91.9	97.2	93.4
Zipper	52.5	91.7	91.1	91.3	95.7	97.0
Tile	34.6	79.1	92.7	94.7	89.5	93.7
Wood	36.1	85.1	95.8	96.4	94.0	95.7
Mean	35.6	82.3	87.6	91.1	89.6	90.5

Table 16. Fine-grained performance comparison for Pixel-level AUROC on MVTec.

Object name	CLIP	WinCLIP	VAND	AnomalyCLIP	AdaCLIP	ViP ² -CLIP
Carpet	6.2	66.3	48.5	90.0	38.1	97.9
Bottle	0.3	69.9	45.6	80.8	39.0	83.5
Hazelnut	4.7	81.4	70.3	92.5	19.4	93.1
Leather	1.4	86.0	72.4	92.2	57.0	98.8
Cable	8.8	39.4	25.7	64.0	43.1	66.5
Capsule	31.6	63.7	51.3	87.6	60.3	92.7
Grid	0.2	49.3	31.6	75.4	57.9	89.5
Pill	5.3	66.9	65.4	88.1	40.5	93.1
Transistor	8.6	45.5	21.3	58.2	27.1	55.1
Metal Nut	0.9	39.6	38.4	71.1	63.9	79.8
Screw	48.5	70.2	67.1	88.0	16.1	94.2
Toothbrush	2.3	67.9	54.5	88.5	58.9	88.8
Zipper	20.8	72.1	10.7	65.4	18.1	89.1
Tile	6.3	54.5	26.7	87.4	25.7	89.2
Wood	12.9	56.3	31.1	91.5	2.4	95.5
Mean	10.6	61.9	44.0	81.4	37.8	87.1

Table 17. Fine-grained performance comparison for Pixel-level AUPRO on MVTec.

Object name	CLIP	WinCLIP	VAND	AnomalyCLIP	AdaCLIP	ViP ² -CLIP
Carpet	3.2	33.9	65.7	57.0	59.5	65.5
Bottle	10.9	49.4	53.4	51.6	32.2	52.3
Hazelnut	4.2	39.1	50.5	47.6	34.2	49.9
Leather	1.3	30.8	50.0	33.2	66.6	43.0
Cable	5.6	12.2	23.9	18.9	37.0	24.1
Capsule	4.8	14.3	33.1	31.0	63.3	34.4
Grid	1.4	13.7	40.8	32.0	49.8	41.3
Pill	7.4	11.8	27.7	35.5	31.2	26.0
Transistor	9.2	27.0	19.0	18.8	31.7	16.0
Metal Nut	21.0	23.8	28.0	33.1	28.6	35.1
Screw	6.4	11.3	41.7	33.4	67.4	46.4
Toothbrush	3.0	10.5	48.1	29.0	47.8	31.9
Zipper	5.2	27.8	40.5	45.0	18.0	53.2
Tile	13.2	30.8	66.5	64.9	52.9	68.0
Wood	7.4	35.4	60.3	55.2	55.6	58.7
Mean	6.9	24.8	43.3	39.1	45.1	43.1

Table 18. Fine-grained performance comparison for Pixel-level F1 on MVTec.

Object name	CLIP	WinCLIP	VAND	AnomalyCLIP	AdaCLIP	ViP ² -CLIP
Carpet	86.9	99.3	99.4	100	99.9	99.9
Bottle	20.5	98.6	91.9	88.7	97.9	93.7
Hazelnut	53	92.3	89.4	97.2	97.2	93.5
Leather	98.5	100	99.7	99.8	99.9	100
Cable	51.4	85	88.1	70.3	65.5	75.3
Capsule	60.7	68.6	79.9	89.5	86.5	90.2
Grid	77	99.2	86.5	97.8	99.4	99.7
Pill	61.2	81.5	80.9	81.1	84.6	84.6
Transistor	45.6	89.1	80.8	93.9	82.2	79.9
Metal Nut	68.2	96.2	68.4	92.4	75.9	77.3
Screw	62.2	71.6	85.1	82.1	97.8	90
Toothbrush	23.6	85.3	53.6	85.3	93.3	94.2
Zipper	90	91.2	89.6	98.4	96.4	92.9
Tile	98.9	99.9	99.9	100	99.9	98.5
Wood	99.6	97.6	99	96.9	99.0	98.6
Mean	66.5	90.4	86.1	91.6	90.1	91.2

Table 19. Fine-grained performance comparison for Image-level AUROC on MVTec.

Object name	CLIP	WinCLIP	VAND	AnomalyCLIP	AdaCLIP	ViP ² -CLIP
Carpet	95.6	97.8	99.8	100	99.9	100
Bottle	65	97.6	97.6	96.8	99.4	98.1
Hazelnut	67.2	88.6	94.6	98.5	98.4	96.8
Leather	99.5	100	99.9	99.9	99.9	100
Cable	66.2	89.8	92.9	81.7	81.8	84.5
Capsule	88.5	90.5	95.4	97.8	97.1	97.9
Grid	90.6	98.2	94.9	99.3	99.8	99.9
Pill	89.9	96.4	96.1	95.3	96.6	96.6
Transistor	46.3	84.9	77.5	92.1	82.7	80
Metal Nut	91.1	99.1	91.8	98.2	94.5	94.7
Screw	81.6	87.7	93.6	92.9	96.5	96.5
Toothbrush	60.7	94.5	71.6	93.9	97.7	97.5
Zipper	96.6	97.5	97.1	99.5	99.1	98.2
Tile	99.5	100	100	100	100	99.5
Wood	99.9	99.3	99.7	99.2	99.7	99.6
Mean	82.6	95.6	93.5	96.4	95.6	96

Table 20. Fine-grained performance comparison for Image-level AP on MVTec.

Object name	CLIP	WinCLIP	VAND	AnomalyCLIP	AdaCLIP	ViP ² -CLIP
Carpet	89.4	97.8	98.3	99.4	99.4	99.4
Bottle	86.3	97.6	92.1	90.9	92.4	92.4
Hazelnut	77.8	88.6	87	92.6	91.2	91.2
Leather	96.7	100	98.9	99.5	99.5	100
Cable	76	84.8	84.5	77.4	76.0	80.2
Capsule	90.5	93.5	91.5	91.7	93.1	93
Grid	88.4	98.2	89.1	97.3	98.3	99.1
Pill	91.6	91.6	91.6	92.1	91.8	91.8
Transistor	57.1	80	73.9	83.7	75.9	71.8
Metal Nut	89.4	95.3	89.4	93.7	89.4	90.3
Screw	85.6	85.9	89.3	88.3	91.3	91.3
Toothbrush	83.3	88.9	83.3	90	93.5	93.5
Zipper	91.5	93.4	90.8	97.9	95.1	92.4
Tile	97	99.4	99.4	100	99.4	96.4
Wood	99.2	95.2	97.4	96.6	96.7	96.8
Mean	86.7	92.7	90.4	92.7	92.3	92

Table 21. Fine-grained performance comparison for Image-level F1 on MVTec.



Figure 11. Anomaly score maps for the data subset, capsule, in MVTec AD. The first row represents the input, the second row presents the segmentation results from ViP²-CLIP.

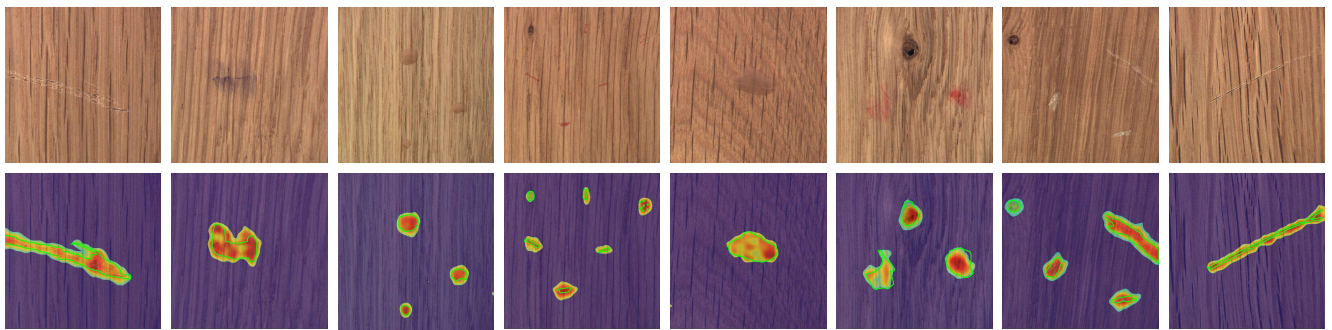


Figure 12. Anomaly score maps for the data subset, wood, in MVTec AD. The first row represents the input, the second row presents the segmentation results from ViP²-CLIP.

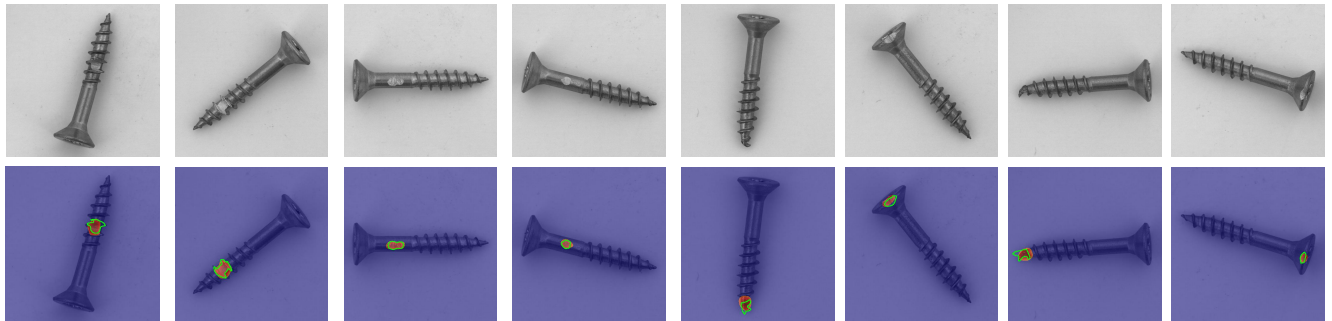


Figure 13. Anomaly score maps for the data subset, screw, in MVTec AD. The first row represents the input, the second row presents the segmentation results from ViP²-CLIP.

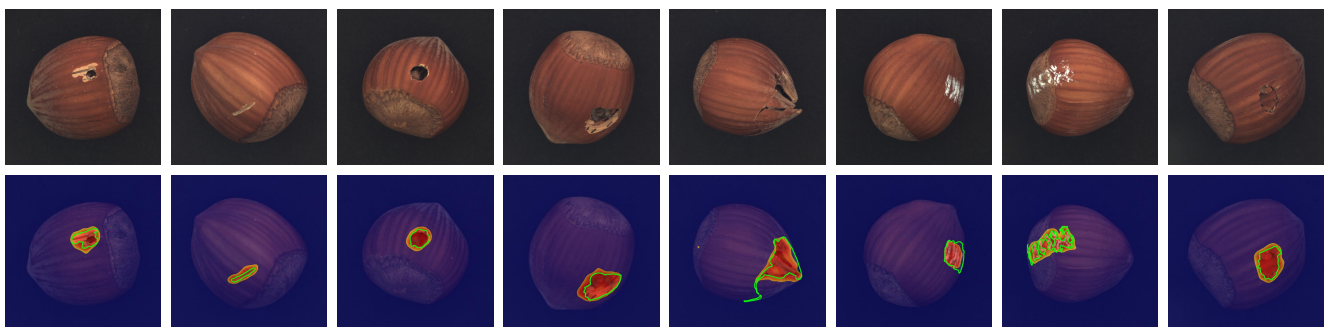


Figure 14. Anomaly score maps for the data subset, hazelnut, in MVTec AD. The first row represents the input, the second row presents the segmentation results from ViP²-CLIP.

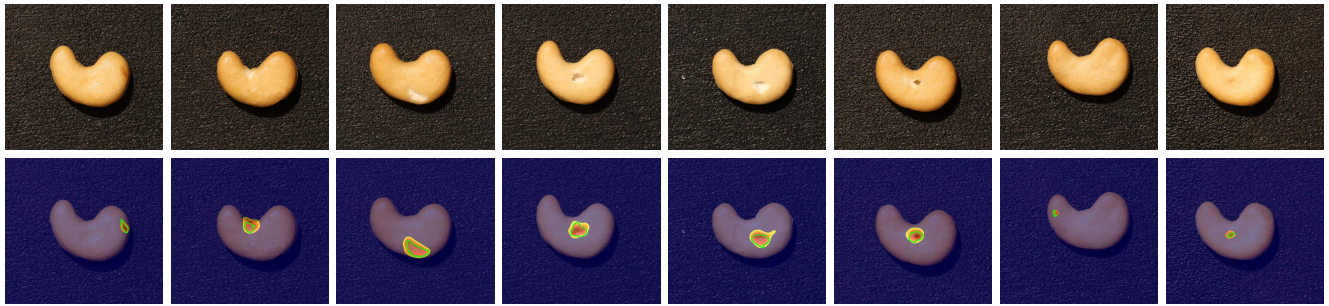


Figure 15. Anomaly score maps for the data subset, cashew, in VisA. The first row represents the input, the second row presents the segmentation results from ViP²-CLIP.

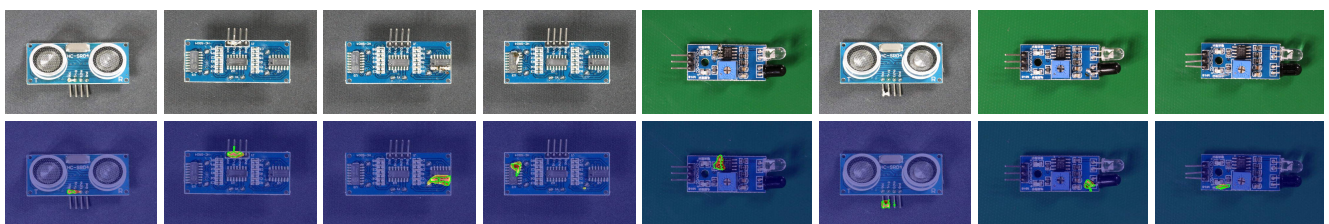


Figure 16. Anomaly score maps for the data subset, pcb, in VisA. The first row represents the input, the second row presents the segmentation results from ViP²-CLIP.

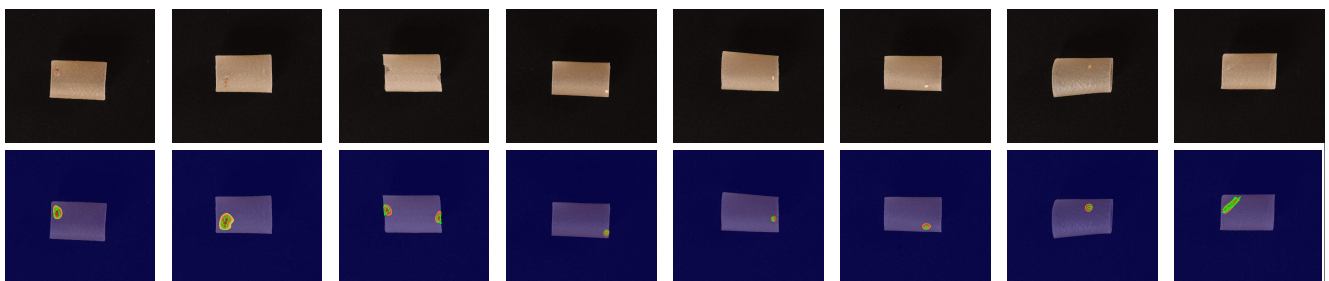


Figure 17. Anomaly score maps for the data subset, pipe fryum, in VisA. The first row represents the input, the second row presents the segmentation results from ViP²-CLIP.

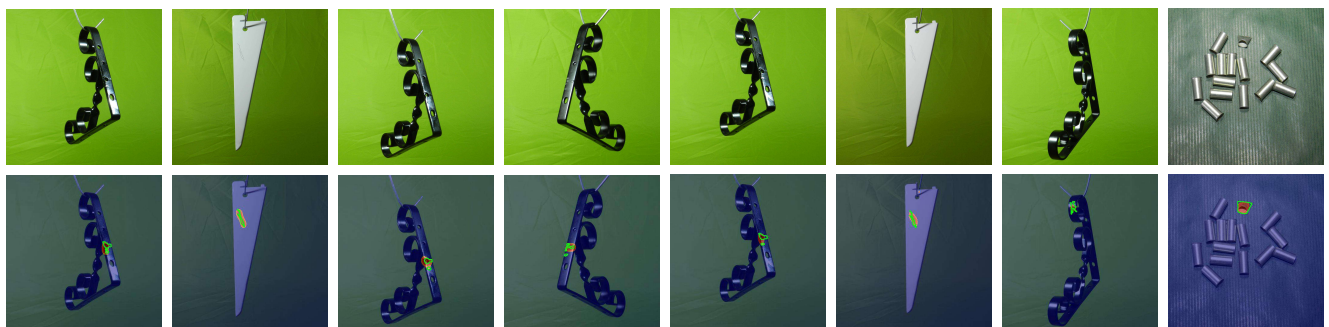


Figure 18. Anomaly score maps for the data subset in MPDD. The first row represents the input, the second row presents the segmentation results from ViP²-CLIP.

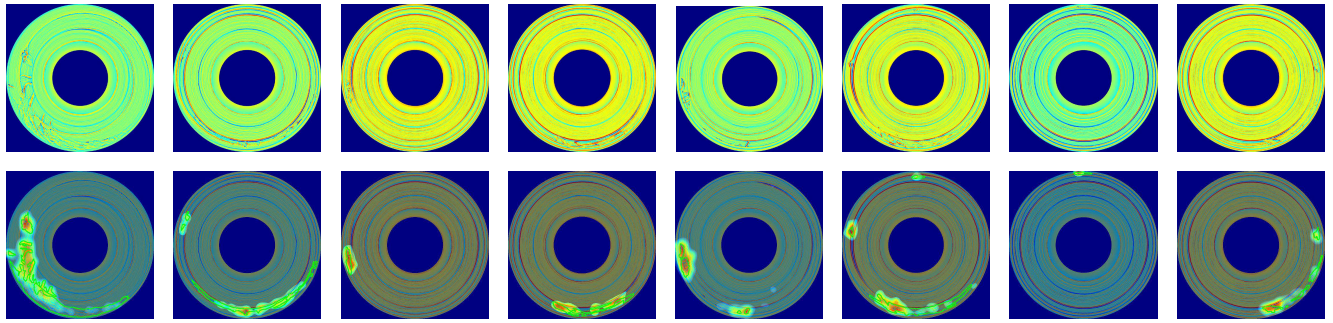


Figure 19. Anomaly score maps for the data subset in BTAD. The first row represents the input, the second row presents the segmentation results from ViP²-CLIP.

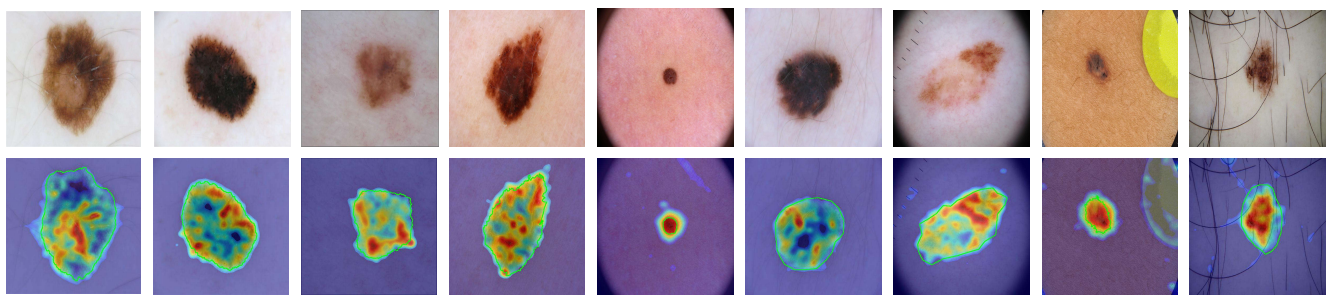


Figure 20. Anomaly score maps for the data subset skin. The first row represents the input, the second row presents the segmentation results from ViP²-CLIP.

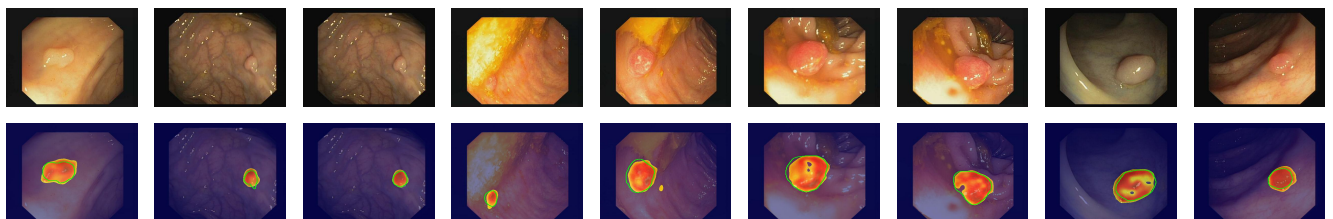


Figure 21. Anomaly score maps for the data subset colon. The first row represents the input, the second row presents the segmentation results from ViP²-CLIP.

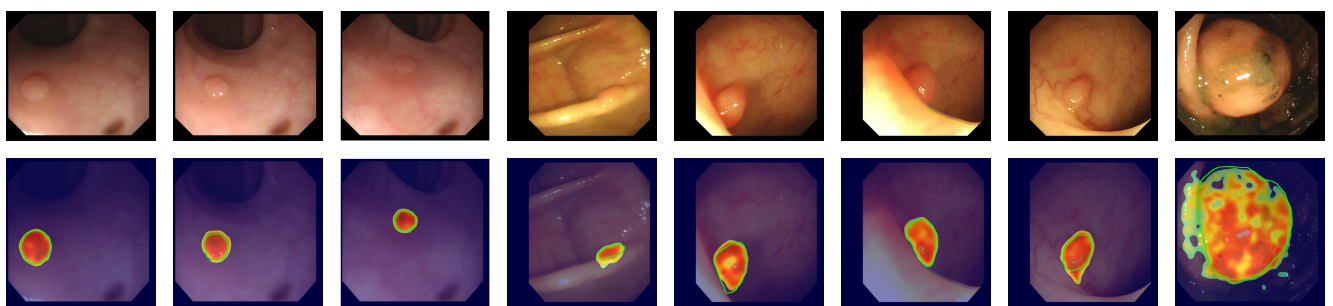


Figure 22. Anomaly score maps for the data subset colon. The first row represents the input, the second row presents the segmentation results from ViP²-CLIP.

References

[1] Toshimichi Aota, Lloyd Teh Tzer Tong, and Takayuki Okatani. Zero-shot versus many-shot: Unsupervised texture anomaly detection. In *Proceedings of the IEEE/CVF Winter Conference on Applications of Computer Vision*, pages 5564–5572, 2023. 5

[2] Paul Bergmann, Michael Fauser, David Sattlegger, and Carsten Steger. Mvttec ad—a comprehensive real-world dataset for unsupervised anomaly detection. In *Proceedings of the IEEE/CVF conference on computer vision and pattern recognition*, pages 9592–9600, 2019. 5

[3] Jorge Bernal, F Javier Sánchez, Gloria Fernández-Esparrach, Debora Gil, Cristina Rodríguez, and Fernando Vilariño. Wm-dova maps for accurate polyp highlighting in colonoscopy: Validation vs. saliency maps from physicians. *Computerized medical imaging and graphics*, 43:99–111, 2015. 5

[4] Yunkang Cao, Jiangning Zhang, Luca Frittoli, Yuqi Cheng, Weiming Shen, and Giacomo Boracchi. Adaclip: Adapting clip with hybrid learnable prompts for zero-shot anomaly detection. In *European Conference on Computer Vision*, pages 55–72. Springer, 2024. 2, 5, 9, 10

[5] Xuhai Chen, Yue Han, and Jiangning Zhang. A zero-few-shot anomaly classification and segmentation method for cvpr 2023 vand workshop challenge tracks 1&2. *1st Place on Zero-shot AD and 4th Place on Few-shot AD*, 2305:17382, 2023. 2, 4, 5, 10

[6] Xuhai Chen, Jiangning Zhang, Guanzhong Tian, Haoyang He, Wuhao Zhang, Yabiao Wang, Chengjie Wang, and Yong Liu. Clip-ad: A language-guided staged dual-path model for zero-shot anomaly detection. In *International Joint Conference on Artificial Intelligence*, pages 17–33. Springer, 2024. 2, 4, 9

[7] Noel CF Codella, David Gutman, M Emre Celebi, Brian Helba, Michael A Marchetti, Stephen W Dusza, Aadi Kalloo, Konstantinos Liopyris, Nabin Mishra, Harald Kittler, et al. Skin lesion analysis toward melanoma detection: A challenge at the 2017 international symposium on biomedical imaging (isbi), hosted by the international skin imaging collaboration (isic). In *2018 IEEE 15th international symposium on biomedical imaging (ISBI 2018)*, pages 168–172. IEEE, 2018. 5

[8] Hanqiu Deng and Xingyu Li. Anomaly detection via reverse distillation from one-class embedding. In *Proceedings of the IEEE/CVF conference on computer vision and pattern recognition*, pages 9737–9746, 2022. 10

[9] Qingqing Fang, Wenxi Lv, and Qinliang Su. Af-clip: Zero-shot anomaly detection via anomaly-focused clip adaptation. *arXiv preprint arXiv:2507.19949*, 2025. 2

[10] Zhaopeng Gu, Bingke Zhu, Guibo Zhu, Yingying Chen, Hao Li, Ming Tang, and Jinqiao Wang. Filo: Zero-shot anomaly detection by fine-grained description and high-quality localization. In *Proceedings of the 32nd ACM International Conference on Multimedia*, pages 2041–2049, 2024. 2

[11] Yuncheng Guo and Xiaodong Gu. Mmrl: Multi-modal representation learning for vision-language models. In *Proceedings of the Computer Vision and Pattern Recognition Conference*, pages 25015–25025, 2025. 2

[12] Ahmed Hamada. BR35H: Brain Tumor Detection 2020. <https://www.kaggle.com/datasets/ahmedhamada0/brain-tumor-detection>, 2020. Accessed: 2025-05-07. 5

[13] Steven A Hicks, Devesh Jha, Vajira Thambawita, Pål Halvorsen, Hugo L Hammer, and Michael A Riegler. The endotect 2020 challenge: evaluation and comparison of classification, segmentation and inference time for endoscopy. In *Pattern Recognition. ICPR International Workshops and Challenges: Virtual Event, January 10-15, 2021, Proceedings, Part VIII*, pages 263–274. Springer, 2021. 5

[14] Jongheon Jeong, Yang Zou, Taewan Kim, Dongqing Zhang, Avinash Ravichandran, and Onkar Dabeer. Winclip: Zero-/few-shot anomaly classification and segmentation. In *Proceedings of the IEEE/CVF Conference on Computer Vision and Pattern Recognition*, pages 19606–19616, 2023. 1, 2, 3, 5, 10

[15] Stepan Jezek, Martin Jonak, Radim Burget, Pavel Dvorak, and Milos Skotak. Deep learning-based defect detection of metal parts: evaluating current methods in complex conditions. In *2021 13th International congress on ultra modern telecommunications and control systems and workshops (ICUMT)*, pages 66–71. IEEE, 2021. 5

[16] D Jha, PH Smedsrød, MA Riegler, P Halvorsen, T De Lange, D Johansen, and HD Johansen. Kvasir-seg: A segmented polyp dataset. multimedia modeling. *MMM 2020. Lecture Notes in Computer Science*, 11962, 2019. 5

[17] Muhammad Uzair Khattak, Hanoona Rasheed, Muhammad Maaz, Salman Khan, and Fahad Shahbaz Khan. Maple: Multi-modal prompt learning. In *Proceedings of the IEEE/CVF conference on computer vision and pattern recognition*, pages 19113–19122, 2023. 2

[18] Muhammad Uzair Khattak, Syed Talal Wasim, Muzammal Naseer, Salman Khan, Ming-Hsuan Yang, and Fahad Shahbaz Khan. Self-regulating prompts: Foundational model adaptation without forgetting. In *Proceedings of the IEEE/CVF international conference on computer vision*, pages 15190–15200, 2023. 2

[19] Chengyuan Li, Suyang Zhou, Jieping Kong, Lei Qi, and Hui Xue. Kanoclip: Zero-shot anomaly detection through knowledge-driven prompt learning and enhanced cross-modal integration. *arXiv preprint arXiv:2501.03786*, 2025. 2, 9

[20] Xiaoya Li, Xiaofei Sun, Yuxian Meng, Junjun Liang, Fei Wu, and Jiwei Li. Dice loss for data-imbalanced nlp tasks. *arXiv preprint arXiv:1911.02855*, 2019. 5

[21] Tsung-Yi Lin, Priya Goyal, Ross Girshick, Kaiming He, and Piotr Dollár. Focal loss for dense object detection. In *Proceedings of the IEEE international conference on computer vision*, pages 2980–2988, 2017. 5

[22] Wenxin Ma, Xu Zhang, Qingsong Yao, Fenghe Tang, Chenxu Wu, Yingtai Li, Rui Yan, Zihang Jiang, and S Kevin Zhou. Aa-clip: Enhancing zero-shot anomaly detection via anomaly-aware clip. In *Proceedings of the Computer Vision and Pattern Recognition Conference*, pages 4744–4754, 2025. 2, 5, 10

[23] Pankaj Mishra, Riccardo Verk, Daniele Fornasier, Claudio Piciarelli, and Gian Luca Foresti. Vt-adl: A vision transformer network for image anomaly detection and localization. In *2021 IEEE 30th International Symposium on Industrial Electronics (ISIE)*, pages 01–06. IEEE, 2021. 5

[24] Long Ouyang, Jeffrey Wu, Xu Jiang, Diogo Almeida, Carroll Wainwright, Pamela Mishkin, Chong Zhang, Sandhini Agarwal, Katarina Slama, Alex Ray, et al. Training language models to follow instructions with human feedback. *Advances in neural information processing systems*, 35:27730–27744, 2022. 2

[25] Zhen Qu, Xian Tao, Mukesh Prasad, Fei Shen, Zhengtao Zhang, Xinyi Gong, and Guiguang Ding. Vcp-clip: A visual context prompting model for zero-shot anomaly segmentation. In *European Conference on Computer Vision*, pages 301–317. Springer, 2024. 1, 2

[26] Alec Radford, Jong Wook Kim, Chris Hallacy, Aditya Ramesh, Gabriel Goh, Sandhini Agarwal, Girish Sastry, Amanda Askell, Pamela Mishkin, Jack Clark, et al. Learning transferable visual models from natural language supervision. In *International conference on machine learning*, pages 8748–8763. PMLR, 2021. 1, 2, 5, 9

[27] Yongming Rao, Wenliang Zhao, Guangyi Chen, Yansong Tang, Zheng Zhu, Guan Huang, Jie Zhou, and Jiwen Lu. Denseclip: Language-guided dense prediction with context-aware prompting. In *Proceedings of the IEEE/CVF conference on computer vision and pattern recognition*, pages 18082–18091, 2022. 2

[28] Karsten Roth, Latha Pemula, Joaquin Zepeda, Bernhard Schölkopf, Thomas Brox, and Peter Gehler. Towards total recall in industrial anomaly detection. In *Proceedings of the IEEE/CVF conference on computer vision and pattern recognition*, pages 14318–14328, 2022. 10

[29] Mohammadreza Salehi, Niousha Sadjadi, Soroosh Baselizadeh, Mohammad H Rohban, and Hamid R Rabiee. Multiresolution knowledge distillation for anomaly detection. In *Proceedings of the IEEE/CVF conference on computer vision and pattern recognition*, pages 14902–14912, 2021. 5

[30] Domen Tabernik, Samo Šela, Jure Skvarč, and Danijel Skočaj. Segmentation-based deep-learning approach for surface-defect detection. *Journal of Intelligent Manufacturing*, 31(3):759–776, 2020. 5

[31] Nima Tajbakhsh, Suryakanth R Gurudu, and Jianming Liang. Automated polyp detection in colonoscopy videos using shape and context information. *IEEE transactions on medical imaging*, 35(2):630–644, 2015. 5

[32] Hugo Touvron, Thibaut Lavril, Gautier Izacard, Xavier Martinet, Marie-Anne Lachaux, Timothée Lacroix, Baptiste Rozière, Naman Goyal, Eric Hambro, Faisal Azhar, et al. Llama: Open and efficient foundation language models. *arXiv preprint arXiv:2302.13971*, 2023. 2

[33] Matthias Wieler and Tobias Hahn. Weakly supervised learning for industrial optical inspection. In *DAGM symposium in*, page 11, 2007. 5

[34] Hantao Yao, Rui Zhang, and Changsheng Xu. Visual-language prompt tuning with knowledge-guided context optimization. In *Proceedings of the IEEE/CVF conference on computer vision and pattern recognition*, pages 6757–6767, 2023. 2

[35] Hantao Yao, Rui Zhang, and Changsheng Xu. Tcp: Textual-based class-aware prompt tuning for visual-language model. In *Proceedings of the IEEE/CVF Conference on Computer Vision and Pattern Recognition*, pages 23438–23448, 2024. 2

[36] Kaiyang Zhou, Jingkang Yang, Chen Change Loy, and Ziwei Liu. Conditional prompt learning for vision-language models. In *Proceedings of the IEEE/CVF conference on computer vision and pattern recognition*, pages 16816–16825, 2022. 2

[37] Qihang Zhou, Guansong Pang, Yu Tian, Shibo He, and Jiming Chen. Anomalyclip: Object-agnostic prompt learning for zero-shot anomaly detection. In *ICLR*, 2024. 1, 2, 4, 5, 10

[38] Yang Zou, Jongheon Jeong, Latha Pemula, Dongqing Zhang, and Onkar Dabeer. Spot-the-difference self-supervised pre-training for anomaly detection and segmentation. In *European Conference on Computer Vision*, pages 392–408. Springer, 2022. 5